High-resolution modelling of early contrail evolution from hydrogen-powered aircraft

Annemarie Lottermoser and Simon Unterstrasser

Deutsches Zentrum für Luft- und Raumfahrt, Institut für Physik der Atmosphäre, Oberpfaffenhofen, Germany

Correspondence: Annemarie Lottermoser (annemarie.lottermoser@dlr.de)

Abstract. In this study, we investigate the properties of young contrails formed behind hydrogen-powered aircraft, particularly compared to contrails from conventional kerosene combustion. High-resolution simulations of individual contrails are performed using the EULAG-LCM model, a large-eddy simulation model with fully coupled particle-based ice microphysics.

Previous studies on early contrail evolution during the vortex phase explored a range of meteorological and aircraft-related

5   parameters but focused on contrails with ice crystal numbers and water vapor emissions typical of kerosene combustion.

This study examines the early H_2-contrail evolution, starting tenths of a second after exhaust emission when ice crystal formation is complete. Two key parameters are adjusted: the emitted water vapor mass and the number of ice crystals formed during the initial stage. The emitted water vapor varies between 3.7 and 38.6 g per flight meter, depending on the fuel and aircraft type. The initial ice crystal number spans four orders of magnitude, from approximately 10^{10} to 10^{14} ice crystals per

10   flight meter. Additionally, we extend our atmospheric scenarios to ambient temperatures up to 235 K, as H_2 contrails can form in warmer conditions where kerosene plumes typically cannot.

Our results show that vortex phase processes reduce the four-order magnitude difference in ice crystal number to two orders of magnitude. Moreover, relative ice crystal loss increases with increasing ambient temperatures and decreasing relative humidity levels.

15   Finally, we extend the parametrization of ice crystal loss from a previous study to include scenarios of contrails from hydrogen propulsion systems.

1 Introduction

For conventional kerosene-powered aircraft, the primary exhaust emissions consist of carbon dioxide and water vapor, with approximately 1.26 kg of water vapor emitted per kilogram of fuel burned (Bier et al., 2024). If the ambient atmosphere is

20   sufficiently cold, water supersaturation emerges due to the mixing of the hot exhaust gases with the cold ambient air (Schumann, 1996). This happens within tenths of a second after the emission of the exhaust. Under these conditions and in the case of soot-rich combustion, water vapor condenses onto soot particles in the exhaust, forming water droplets that grow and eventually freeze into contrail ice crystals by homogeneous nucleation (Kärcher et al., 2015). In ice-supersaturated conditions, these young (i.e. several minutes old) line-shaped contrails can evolve into contrail-cirrus, which may persist for several hours (Lewellen

25   et al., 2014; Unterstrasser et al., 2017a). Contrail-cirrus has been identified as a significant contributor to aviation-induced

radiative forcing. On a global scale, contrail-cirrus exert a positive radiative forcing, resulting in a net warming effect on the atmosphere (Burkhardt and Kärcher, 2011; Lee et al., 2021; Bier and Burkhardt, 2022).

Several contrail mitigation strategies are currently under debate, and their mitigation potential is estimated. Adaptations of flight routes can pursue avoiding ice-supersaturated regions, where contrail formation and persistence are likely to happen (Gierens et al., 2020; Lee et al., 2023). Flying in formation reduces the contrail climate impact due to saturation effects (Marks et al., 2021; Unterstrasser, 2020). Moreover, modifying the fuel composition (e.g. by using sustainable aviation fuels (SAFs)) can reduce the number of emitted soot particles (Moore et al., 2017). Measurements have demonstrated that using alternative fuel blends can reduce the number of ice crystals formed as the contrail ice crystals primarily form on the emitted exhaust particles (Bräuer et al., 2021; Voigt et al., 2021). Märkl et al. (2024) find, in the specific case of the ECLIF3 experiment, a 56 % reduction in ice particle number per mass of burnt fuel for 100 % SAF compared to a reference Jet A-1 fuel. The initial ice crystal number is the crucial quantity that controls the contrail radiative effect and life cycle for given meteorological conditions (Unterstrasser and Gierens, 2010; Burkhardt et al., 2018). A systematic reduction of the ice crystal number in contrail-cirrus, e.g. triggered by using SAFs, decreases their optical depth and, consequently, their global radiative forcing (Bier et al., 2017; Burkhardt et al., 2018). However, Burkhardt et al. (2018) have found that the relationship between ice crystal number in young contrails and the climate impact of contrail-cirrus is nonlinear. Consequently, recent advancements are being explored to reduce the number of emitted particles even further, such as transitioning to hydrogen-powered aircraft. As part of the ZEROe project, Airbus plans to build the first commercial hydrogen-powered aircraft by 2035 (Airbus, 2020).

Hydrogen combustion results in exhaust plumes that are significantly moister than kerosene plumes (containing approximately 2.6 times more water vapor), and entrained atmospheric background aerosol particles are expected to serve as contrail ice nuclei, as hydrogen exhaust plumes are void of soot particles (Kärcher et al., 2015; Bier et al., 2024). Recent research by Bier et al. (2024) indicates that hydrogen-powered aircraft could reduce the number of ice crystals formed in contrails by more than 80-90 % compared to kerosene contrails. While no soot particles are produced during hydrogen combustion, the formation of ultrafine volatile particles is possible (Ungeheuer et al., 2022), and their role in ice crystal formation is not yet understood.

Another technological option using hydrogen as an energy carrier employs a hydrogen fuel cell propulsion system (also proposed in the ZEROe project). Hydrogen fuel cells create electrical energy that turns a propeller or fan. Fuel cells offer several advantages over conventional combustion-based technologies as they are expected to operate at a higher overall propulsion efficiency (Kazula et al., 2023). Moreover, hydrogen fuel cells eliminate emissions of carbon dioxide and nitrogen oxides. Despite ongoing development efforts, several uncertainties regarding the performance and operation of fuel cell propulsion systems remain, making this an active field of research. According to the contrail formation theory for fuel cells (Gierens, 2021), the supersaturation over water in the exhaust plume of such systems could be significantly higher than for conventional combustion systems. This leads to a much larger slope of the mixing line as described by the Schmidt-Appleman theory (Schumann, 1996), which defines the linear relationship between plume partial water vapor pressure and temperature. The plume supersaturation can attain very high values, which could trigger homogeneous droplet nucleation (HDN; Wölk and Strey, 2001) and the formation of numerous small water droplets (Jansen and Heymsfield, 2015). Given the low ambient temperatures at typical cruise altitudes, these droplets would rapidly freeze, potentially resulting in a very high initial number

of ice crystals. In this study, we address the potential implications of this propulsion system by artificially increasing the initial number of ice crystals in our simulations. We emphasize that we do not state that fuel cell propulsion leads to a high number of contrail ice crystals. Moreover, there are design options under consideration that may avoid abundant ice crystal production. Hence, our scenarios with high ice crystal numbers should be interpreted just as one possible scenario of fuel cell propulsion.

65   The initial properties of contrails, such as the number of ice crystals, are crucial for evaluating the radiative properties of contrail-cirrus. For a thorough assessment of contrail mitigation options that aim to reduce the number of ice crystals during the initial formation stage, it is essential to examine the implications of the formation processes and consider the subsequent evolution of the contrail during the vortex phase. The vortex phase covers the first few minutes in the contrail's lifetime. The primary process is the interaction of the contrail ice crystals with the descending counter-rotating vortex pair. This consideration

70 is necessary because the initial contrail ice crystal number closely matches the emitted soot particle number only under low temperature and high supersaturation conditions (Bier and Burkhardt, 2022). In contrast, significant deviations can occur under weakly supersaturated conditions and high ambient temperatures. Adiabatic heating in the descending vortex pair increases the saturation pressure, lowering the plume relative humidity. This may lead to the sublimation of the ice crystals trapped in the descending vortices (Lewellen and Lewellen, 2001; Unterstrasser and Sölch, 2010). The survival fraction of ice crystals

75 after the vortex phase is highly influenced by factors such as the number of nucleated ice crystals, the amount of emitted water vapor, ambient temperature, relative humidity over ice, Brunt-Väisälä frequency, and the aircraft's wingspan. Generally, the fraction of ice crystals lost during the vortex phase is larger/smaller, the more/fewer ice crystals are present in the beginning. The initial number of ice crystals is related to the aircraft's fuel flow rate and an assumed apparent ice crystal emission index EI_{iceno} (Unterstrasser and Sölch, 2010; Lewellen et al., 2014). Unterstrasser (2016) states that an initial reduction of EI_{iceno}

80 from 10^{15} to $10^{14}\,kg^{-1}$ implies only a factor 5.3 reduction of the ice crystal number after the vortex phase. Hence, initial differences in the ice crystal number (e.g. by changes in the fuel or engine/combustor design) are reduced during the vortex phase. This means that a decreased ice crystal loss in the vortex phase partly compensates for the reduced ice nucleation (Bier and Burkhardt, 2022). The consideration of ice crystal loss processes during the vortex phase, as parametrized in Unterstrasser (2016) and implemented in larger scale models, lead to significant changes in the later contrail properties on regional (Gruber

85 et al., 2018) and global scale (Bier and Burkhardt, 2022).

    In this study, we systematically investigate the properties of young H_2 contrails with a focus on various ambient and meteorological parameters. In Sec. 2, we present the model and the parameter setup. Section 3 focuses on the sensitivity of H_2 contrails to various parameters. Also, we present the updated parametrization in this section. Implications of the simulation results are discussed in Sec. 4, and conclusions are drawn in Sec. 5.

90 ## 2   Methods

In this section, we introduce our model (Sec. 2.1) and describe the numerical setup employed in our simulations (Sec. 2.2). Furthermore, we define the specific quantities necessary for evaluating and analyzing the results (Sec. 2.3).

2.1 Model

We perform simulations of H$_2$ contrails using the LES model EULAG-LCM. The base LES code EULAG solves the anelastic
formulation of the momentum and energy equations (Smolarkiewicz and Margolin, 1997; Prusa et al., 2008). The microphysical
module LCM, which incorporates a Lagrangian particle-tracking method, has been coupled to EULAG (Sölch and Kärcher,
2010), resulting in the model version EULAG-LCM. This model version has been used in multiple previous studies to explore
the properties of young contrails during the vortex phase (e.g. Unterstrasser and Sölch, 2010; Unterstrasser, 2014; Unterstrasser
and Stephan, 2020) and their transition into contrail-cirrus (Unterstrasser et al., 2017a, b; Unterstrasser, 2020). The model
results have also been used to develop a parametrization of ice crystal loss and the geometric depth of contrails after vortex
break-up (Unterstrasser, 2016).

In the particle-based framework of LCM, ice crystals are represented by simulation particles. Each simulation particle (SIP)
represents a certain number of real ice crystals (referred to as the weight of the SIP) with identical properties, such as size and
mass. The effect of particle inertia, specifically centrifugal acceleration in the rotating wake vortices, is neglected due to the
small ice crystal sizes present in the primary wake, as shown in Unterstrasser (2014).

In this study, we consider the deposition growth and sublimation of ice crystals and latent heat release to be the most
important microphysical processes and switch off several LCM routines, such as aggregation and radiation.

2.2 Numerical setup and set of simulations

Generally, we assume ambient conditions such that contrails form and persist, i.e. the atmosphere is sufficiently cold and moist
(Schumann, 1996; Gierens and Spichtinger, 2000).

As hydrogen propulsion technology is likely to be initially employed on smaller aircraft, we conduct simulations for both
an aircraft with a wing span of 60.3 m (A350/B777-like aircraft, default) and a smaller aircraft with a wing span of 34.4 m
(A320/B737-like aircraft). Generally, the setups are consistent with a previous EULAG-LCM study, where contrails from six
different aircraft types were systematically investigated (Unterstrasser and Görsch, 2014). Throughout the text, when we use
"A350" ("A320") aircraft, we are specifically referring to an "A350/B777-like" aircraft ("A320/B737-like" aircraft).

The number of grid points in our default model domain is $n_x = 384$, $n_y = 200$, and $n_z = 600$, where x, y, and z denote
the transverse, longitudinal (along flight direction), and vertical direction, respectively. The size of the simulation domain is
adjusted based on specific conditions. For example, weaker stratification requires a larger domain, as the vortices descend
further and exhibit more pronounced meandering due to the Crow instability (Crow, 1970). Additionally, for high cruise-
altitude temperatures (i.e. $T_{CA} = 230, 233$, and 235 K), the vertical domain size was increased from 600 to 800 grid points
for the A350, and from 856 to 1112 grid points for the A320. The grid resolution is 1 m along the transverse and vertical
and 2 m along the longitudinal direction. For simulating an A320 aircraft, the resolution is changed to $dx = dz = 0.57$ m and
$dy = 1.14$ m as described in Unterstrasser and Görsch (2014). For both aircraft types, the domain size in flight direction is
chosen to allow the formation of the most unstable Crow mode. Periodic boundary conditions are applied in the horizontal
and longitudinal directions. In the vertical direction, rigid boundary conditions are used, meaning that the vertical velocity

component is zero at the top and bottom boundaries of the simulation domain. The total simulated time is around six to seven minutes, where the time step increases from initially 0.03 s to 0.08 s at later stages of the simulation.

The simulations start at a plume age of several seconds. At this stage, it can be assumed that the ice crystal formation is finished and the vortices have fully rolled up. We initialize the ice crystals in two discs (one per wing) with uniform ice crystal number concentrations. The flow field is a superposition of a turbulent background field and two counter-rotating Lamb-Oseen vortices. The vortex circulation, vortex core radius, and plume radius depend on the aircraft type and are given in Tab. 1.

We incorporate the effects of a hydrogen propulsion system by varying the initial number of ice crystals N_0 and the emitted water vapor mass I_0. The default values of the initial ice crystal number correspond to typical values of the fuel flow rate, denoted by $\dot{m}_F$, and an apparent ice emission index $\mathrm{EI}_{\mathrm{iceno}} = 2.8 \times 10^{14}\,\mathrm{kg}^{-1}$ (Unterstrasser and Görsch, 2014), which represents a typical kerosene contrail. N_0 is then determined by

$$N_0 = m_C \times \mathrm{EI}_{\mathrm{iceno}}, \tag{1}$$

where the fuel consumption m_C is defined as $m_C := \dot{m}_F / U_\infty$. U_∞ represents the aircraft velocity. The reference values are $N_{0,\mathrm{ref}} = 0.85 \times 10^{12}\,\mathrm{m}^{-1}$ for an A320 aircraft and $3.38 \times 10^{12}\,\mathrm{m}^{-1}$ for an A350 aircraft.

To explore a broad range of scenarios, we scale N_0 up and down by factors of 10 and 100 relative to $N_{0,\mathrm{ref}}$. The downscaling simulations are supposed to cover hydrogen combustion scenarios. Conversely, the upscaling simulations could represent scenarios involving a hydrogen fuel cell propulsion system with HDN occurring (see Sec. 1). Varying the number of ice crystals in the model is achieved by varying the weight of the SIPs, which keeps their total number roughly the same. Clearly, the assumptions on the initial ice crystal number are made for hypothetical aircraft designs, and the research on contrail formation processes in H_2 plumes started only recently (Bier et al., 2024; Ponsonby et al., 2024). A more in-depth discussion of the representativity of our N_0 choice is deferred to Sec. 4.

Analogously to N_0, the emitted water vapor mass is calculated using

$$I_0 = m_C \times \mathrm{EI}_{\mathrm{H_2O}}, \tag{2}$$

where $\mathrm{EI}_{\mathrm{H_2O}}$ is the emission index of water vapor, with a value of $1.26\ \mathrm{kg\,kg}^{-1}$ for all aircraft types (Bier et al., 2024). We increase I_0 by multiplying the default values, $3.7\,\mathrm{g\,m}^{-1}$ for an A320 aircraft and $15.0\,\mathrm{g\,m}^{-1}$ for an A350 aircraft (referred to as $I_{0,\mathrm{kero}}$), with 2.57 resulting in $9.51\,\mathrm{g\,m}^{-1}$ and $38.55\,\mathrm{g\,m}^{-1}$ (referred to as $I_{0,\mathrm{H_2}}$), respectively. The value of 2.57 corresponds to the ratio of the emission index of water vapor divided by the combustion heat Q of hydrogen to kerosene (Bier et al., 2024). Note that N_0 and I_0 are given in units "per meter of flight path". Table 2 summarizes the key differences between hydrogen and kerosene fuel and exhaust properties.

We want to mention one caveat that is crucial for properly interpreting the comparison between the H_2 and kerosene scenarios. According to Tab. 2, switching from kerosene to H_2, the water vapor emission index increases by a factor 7.1, while the specific heat of combustion is higher by a factor of 2.79. The energy-specific water emission is then 2.57 times higher, which is, by the way, a crucial difference affecting the contrail formation process and potential contrail coverage (Schumann, 1996; Bier et al., 2024; Kaufmann et al., 2024). Achieving the same work rate with both fuel types, the hydrogen fuel consumption

is 2.79 times lower, and the water vapor emission (per flight distance) I_0 is 2.57 times larger. Moreover, it is our design choice to assume the same $N_{0,\text{ref}}$ value for both fuel scenarios. This implies that the reference apparent ice emission index $\text{EI}_{\text{iceno,ref}}$ of the H_2 scenarios (i.e. those simulations with higher I_0 values) is actually larger by a factor of 2.79. Comparing a factor "100 down" simulation with larger I_0 values (as a typical representative of a H_2 contrail) with a conventional kerosene contrail (i.e. reference N_0 and smaller I_0 values), must not be interpreted as a factor-100 variation of $\text{EI}_{\text{iceno,ref}}$. The difference is actually smaller (factor ~ 36).

Following e.g. Unterstrasser and Sölch (2010), the initial ice crystal size distribution is represented by a lognormal distribution with a width parameter r_{SD}. We adopt a default value of $r_{\text{SD}} = 3.0$ and explore variations with a narrower ($r_{\text{SD}} = 1.0$, monodisperse) and broader ($r_{\text{SD}} = 4.0$) initial size distribution, as previous studies have identified this parameter as significant (Unterstrasser and Sölch, 2010; Unterstrasser, 2014). Note that other modelling studies that initialize the contrails at an earlier state without the specification that all emitted water vapor has already been deposited on the ice crystals show a weaker impact of the width parameter (Lewellen et al., 2014). We conducted simulations only with a 100-fold increase or decrease when altering the width parameter (to reduce the number of simulations).

Figure 1 shows the mean ice crystal radius versus the initial number of ice crystals for kerosene and hydrogen water vapor emission. For this estimate, we use a density of ice, $\rho_{\text{i}} = 0.92\,\text{g\,cm}^{-3}$, and assume spherical particles, which is a reasonable approximation for small ice crystals with aspect ratios close to one. The radius corresponding to the mean particle mass, r_0, is then approximated by $\sim \left(\frac{I_0}{\rho_{\text{i}} N_0}\right)^{1/3}$, assuming that all emitted water vapor is deposited onto the ice crystals. While the LCM represents ice crystal habits as hexagonal columns, this simplified estimate for r_0 serves as a first-order approximation to illustrate the general relationship between N_0, I_0, and the resulting crystal size. A higher N_0 value generally results in a smaller mean radius because the total amount of water is distributed among more particles. It is also evident that the initial water content I_0 directly affects the initial particle size: the higher I_0 (indicated by triangles that represent the hydrogen case), the larger the initial particles. The initial mean ice crystal radii remain unaffected by a variation in the initial width of the size distribution r_{SD}.

Additionally, we investigate the influence of different atmospheric conditions on the evolution of contrail ice crystals. Previous research has highlighted the importance of ambient temperature at cruise altitude T_{CA}, ambient relative humidity with respect to ice $RH_{\text{i,amb}}$, and atmospheric stratification N_{BV} (described by the Brunt-Väisälä frequency) as key input parameters (Lewellen et al., 2014; Unterstrasser, 2016). We vary these parameters as outlined in Tab. 1. At the lower boundary of the simulation domain, we prescribe an air pressure of $p_0 = 250\,\text{hPa}$ and an air density of approximately $\rho_{\text{air,0}} = 0.4\,\text{kg\,m}^{-3}$. For ambient temperature, we prescribe cruise-altitude values of $T_{\text{CA}} = 217, 225, 230, 233,$ and $235\,\text{K}$. The relative humidity with respect to ice is assumed to be constant throughout the entire simulation domain and set to either 110 or 120 %. We use a background turbulence field with an eddy dissipation rate of $\epsilon = 10^{-7}\,\text{m}^2\,\text{s}^{-3}$. The pressure and temperature vertical profiles are computed for an atmosphere with a vertically constant Brunt-Väisälä frequency according to Eq. 2 in Clark and Farley (1984). At cruise altitude, the resulting air pressure ranges from 231 to 235 hPa, depending on Brunt-Väisälä frequency and temperature. In Tab. 1, an average air pressure value is provided. It would seem appropriate to vary ambient pressure in combination with T_{CA} to reflect a change in flight altitude. However, a variation of pressure has only little impact on the simulated contrail

Aircraft and vortex parameters			Ice crystal parameters			
	A320/B737	A350/B777*			A320/B737	A350/B777
b_{span} / m	34.4	60.3	N_0 / ($[10^{10}, 10^{11}, 10^{12*}, 10^{13}, 10^{14}]$ m^{-1})		0.85	3.38
Γ_0 / (m^2 s^{-1})	240	520	I_0 / (10^{-3} kg m^{-1})		$[3.7^*, 9.51]$	$[15.0^*, 38.55]$
r_c / m	3.0	4.0	r_{SD}		$[1.0, 3.0^*, 4.0]$	
r_{plume} / m	12	20				
Atmospheric conditions			Numerical parameters			
$\rho_{air,CA}$ / (kg m^{-3})	0.36				A320/B737	A350/B777
p_{CA} / (10^2 Pa)	233		dx, dy, dz / m		0.57, 1.14, 0.57	1, 2, 1
T_{CA} / K	$[217^*, 225, 230, 233, 235]$		n_x, n_y, n_z		384-768, 200, 600-1112	
$RH_{i,amb}$ / %	$[110, 120^*]$		t_{sim} / s		≈ 400	
ϵ / (m^2 s^{-3})	10^{-7}		dt / s		0.03 - 0.08	
N_{BV} / (10^{-2} s^{-1})	$[0.5, 1.15^*]$					

Table 1. Aircraft/vortex, ice crystal, atmospheric, and numerical parameters. Multiple values in square brackets refer to sensitivity studies, and values with a star refer to default values. b_{span}: wingspan; Γ_0: circulation; r_c: vortex core radius; r_{plume}: plume radius at initialization; N_0: initial number of ice crystals; I_0: emitted water vapor mass; r_{SD}: width of initial ice crystal size distribution; $\rho_{air,CA}$: air density at cruise altitude; p_{CA}: air pressure at cruise altitude; T_{CA}: ambient temperature at cruise altitude; $RH_{i,amb}$: ambient relative humidity with respect to ice; ϵ: eddy dissipation rate; N_{BV}: Brunt-Väisälä frequency; dx, dy, dz: mesh sizes; n_x, n_y, n_z: number of grid points; t_{sim}: simulated time; dt: time step.

properties as demonstrated in Sec. 3.3 in the supplement. This is because the background water vapor mass concentration is independent of ambient pressure. Hence, we do not adapt p_0.

In Tab. 1, values that are marked with a star refer to the default simulation of an A350 aircraft with a water vapor emission that corresponds to a kerosene combustion system $I_0 = 15.0$ g m^{-1} and initial ice crystal number $N_0 = 3.38 \times 10^{12}$ m^{-1} at ambient temperature of 217 K, ambient relative humidity with respect to ice of 120 %, and a standard value for atmospheric stability of 1.15×10^{-2} s^{-1}. Ice crystal formation is improbable for ambient temperatures exceeding 233 K, as this surpasses the homogeneous freezing temperature (Bier et al., 2024), and liquid droplets that form first in the cooling exhaust plume would not freeze. Nevertheless, we include simulations with ambient temperatures of 233 K and 235 K as limiting cases, as droplet freezing in turbulent and quickly cooling plumes is not well-constrained. An overview of all performed simulations is provided in Tab. A1.

2.3 Quantities of interest

In the following, we give definitions of quantities that are used throughout the paper.

fuel/exhaust parameters	hydrogen	kerosene	ratio
$EI_{H_2O} / (\mathrm{kg\,kg^{-1}})$	**8.94**	1.26	7.10
$Q / (10^6\,\mathrm{J\,kg^{-1}})$	**120**	43	2.79
$EI_{H_2O}\,Q^{-1} / (10^{-6}\,\mathrm{kg\,J^{-1}})$	**0.075**	0.029	2.57
	A320/B737		
$m_C / (10^{-3}\,\mathrm{kg\,m^{-1}})$	1.06	2.96	2.79^{-1}
$I_0 / (10^{-3}\,\mathrm{kg\,m^{-1}})$	9.51	3.7	2.57
$N_{0,\mathrm{ref}} / (10^{12}\,\mathrm{m^{-1}})$	0.85	0.85	1
$EI_{\mathrm{iceno,ref}} / (10^{14}\,\mathrm{kg^{-1}})$	7.81	2.8	2.79
	A350/B777		
$m_C / (10^{-3}\,\mathrm{kg\,m^{-1}})$	4.3	12.0	2.79^{-1}
$I_0 / (10^{-3}\,\mathrm{kg\,m^{-1}})$	38.55	15.0	2.57
$N_{0,\mathrm{ref}} / (10^{12}\,\mathrm{m^{-1}})$	3.38	3.38	1
$EI_{\mathrm{iceno,ref}} / (10^{14}\,\mathrm{kg^{-1}})$	7.81	2.8	2.79

Table 2. Fuel, engine, and exhaust parameters for hydrogen propulsion (second column), kerosene (third column) and the ratio between both (fourth column). The water vapor mass emission index and specific heat of combustion ("lower calorific value") are based on Tab. 1 of Schumann (1996).
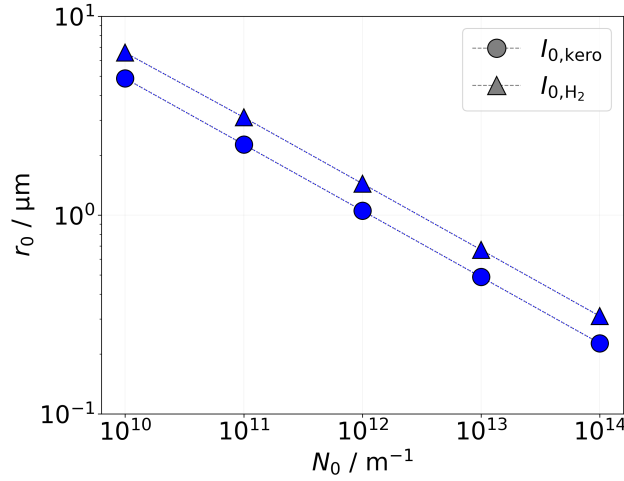

Figure 1. Mean initial ice crystal radius as a function of the initial number of ice crystals. Its sensitivity regarding the microphysical initialization in terms of I_0 (symbol) is depicted.

The total number of ice crystals per meter of flight path and the vertical ice crystal number profile are defined as

$$N_{\text{tot}}(t) = \frac{1}{L_y} \iiint N(x,y,z,t)\,\mathrm{d}x\,\mathrm{d}y\,\mathrm{d}z \quad \text{and} \tag{3}$$

$$N_{\text{v}}(z,t) = \frac{1}{L_y} \iint N(x,y,z,t)\,\mathrm{d}x\,\mathrm{d}y. \tag{4}$$

Both quantities are averaged along flight direction. The total ice mass M_{tot} and the vertical ice mass profile M_{v} are computed analogously. The normalized ice crystal number is calculated as

$$f_N(t) = \frac{N_{\text{tot}}(t)}{N_0}. \tag{5}$$

In Sec. 3, we will use the term "survival fraction of ice crystals" $f_{N,\text{s}}$, which is the normalized ice crystal number at the end of the simulation. Another pertinent quantity to examine is the number of sublimated ice crystals N_{subl}. Vertical normalized profiles $f_{N,\text{v,subl}}$ are computed as described in Eqs. 3-5 and track the number of ice crystals that sublimate at a specific altitude.

3 Results

3.1 Exploring H$_2$ contrails

In this section, we examine the impact of the initial number of ice crystals and the emitted water vapor mass, corresponding to an H$_2$ combustion engine or a potential fuel cell setup. These two parameters are varied as described in Sec. 2.2. The simulations presented in this section are performed for an A350 aircraft at $T_{\text{CA}} = 217\,\text{K}$, $RH_{\text{i,amb}} = 120\,\%$, and $N_{\text{BV}} = 1.15 \times 10^{-2}\,\text{s}^{-1}$, which were also the baseline meteorological conditions in previous EULAG-LCM studies. Hence, this scenario is well-explored and the new simulations build upon the existing ones. Unless stated otherwise, the presented results use the default initial values (indicated by a star in Tab. 1).

Figure 2 (top row) illustrates the temporal evolution of contrail ice crystals in the x,z-plane over a six-minute period. The ice crystal number concentration is averaged along the flight direction. At the start of the simulation, two circular plumes are initialized at $z = 0\,\text{m}$. The centers of the plumes and of the wake vortices are collocated on each side. Within the first two minutes, a downward motion of the ice crystals is observed as the aircraft exhaust descends with the downward moving vortices, forming the primary wake. Also, we see a horizontal broadening of the contrail after few minutes due to the Crow instability (Crow, 1970). Ice crystals that are continuously detrained from the descending exhaust form a curtain between the original emission altitude and the vortex location, known as the secondary wake (Sussmann and Gierens, 1999; Unterstrasser, 2014). After six minutes, ice crystals are visible close to or even above the cruise altitude as the vertically displaced air masses rise back due to buoyancy after vortex break-up. Whereas ice crystals in the secondary wake grow in size due to the deposition of the available water vapor, a significant portion of the ice crystals can sublimate in the primary wake because of adiabatic heating (Sussmann and Gierens, 1999; Lewellen and Lewellen, 1996; Unterstrasser, 2016).

The second row in Fig. 2 shows the cross-sectional ice crystal number concentrations after six minutes for the reference N_0-case ($N_0 = 3.38 \times 10^{12}\,\text{m}^{-1}$) and the N_0-upscaling and N_0-downscaling cases. Higher final number concentrations in

absolute terms are evident in the upscaling cases ($N_0 = 3.38 \times 10^{13}\,\mathrm{m}^{-1}$ and $N_0 = 3.38 \times 10^{14}\,\mathrm{m}^{-1}$). Nonetheless, relative to the initial number, fewer ice crystals survive in these cases, as illustrated in the third row, where the final vertical profiles of normalized ice crystal numbers (green curves) are depicted. This observation is further supported by the final vertical profiles of normalized sublimated ice crystal numbers (orange curves). In the upscaling cases, ice crystals begin to sublimate at higher altitudes because they are smaller in size (see Fig. 1); a phenomenon that has already been described by Huebsch and Lewellen (2006) and Unterstrasser (2014).

Figures 3(a) and (b) display the temporal evolution of the normalized total ice crystal number and absolute total ice mass for different N_0- and I_0-values. The most significant reductions in f_N occur in the upscaling scenarios (red curves in Fig. 3(a)), while the N_0-downscaling simulations (blue curves) show little to no reduction in the temporal evolution of f_N. Due to a higher absolute number of surviving ice crystals in the upscaling cases, these scenarios also exhibit a larger final total ice mass (red curves lie above the blue ones in Fig. 3(b)). The greater loss of ice crystals in the upscaling scenarios is reflected in the survival fraction depicted in Fig. 3(c). Conversely, contrails with a lower value of N_0 (and thus larger initial crystals) are less prone to sublimation, resulting in a higher survival fraction. This implies that initial differences in ice crystal number diminish over time. In this specific scenario, initial differences spanning four orders of magnitude (with N_0-scaling factors of 0.01 and 100) reduce to just two orders of magnitude (0.015 and 7.5) after the vortex phase. Moreover, initializing with a greater amount of emitted water vapor (indicated by circles in Fig. 3(c)) results in larger ice crystal sizes (refer to Fig. 1), which in turn increases the survival fraction and ice mass. In the I_{0,H_2} simulations, the reduction in initial differences is less pronounced, with the four orders of magnitude difference reducing to three orders by the end of the vortex phase.

3.2   Parameter study of H_2-contrail properties

3.2.1   Sensitivity to ambient conditions

As revealed in previous studies, the evolution of contrail ice crystal number and ice mass is highly sensitive to ambient conditions (Lewellen and Lewellen, 2001; Unterstrasser, 2016). This section investigates the impact of ambient relative humidity, temperature, and atmospheric stratification on H_2-contrail properties. Note that we performed simulations at $T_{\mathrm{CA}} \geq 230\,\mathrm{K}$ only for H_2 contrails with an increased I_0 value as the formation of kerosene contrails is unlikely at these high ambient temperatures. The results presented in this section refer to simulations of an A350 aircraft with an initial size distribution width of $r_{\mathrm{SD}} = 3.0$.

In Fig. 4, final vertical profiles of the ice crystal mass and normalized number and survival fractions (after approximately six minutes) are depicted. Columns represent simulations at temperatures of 217 K, 225 K, 230 K, 233 K, and 235 K, respectively. The simulations shown in the first and second rows are performed with $I_0 = I_{0,\mathrm{H}_2}$. The ice mass (first row (1)) remains largely unaffected by variations in N_0, except the factor 100 downscaling simulation, which shows a significantly reduced ice mass. A notable increase in ice mass is observed with increasing temperature, attributable to a higher water vapor mass concentration in the atmosphere. This additional water vapor can be deposited onto the ice crystals, thereby increasing their size.

When examining the normalized ice crystal number (second row (2)), we observe a reduction with increasing temperature, primarily in the primary wake. Although the ice crystals grow larger during the first seconds due to the higher water vapor
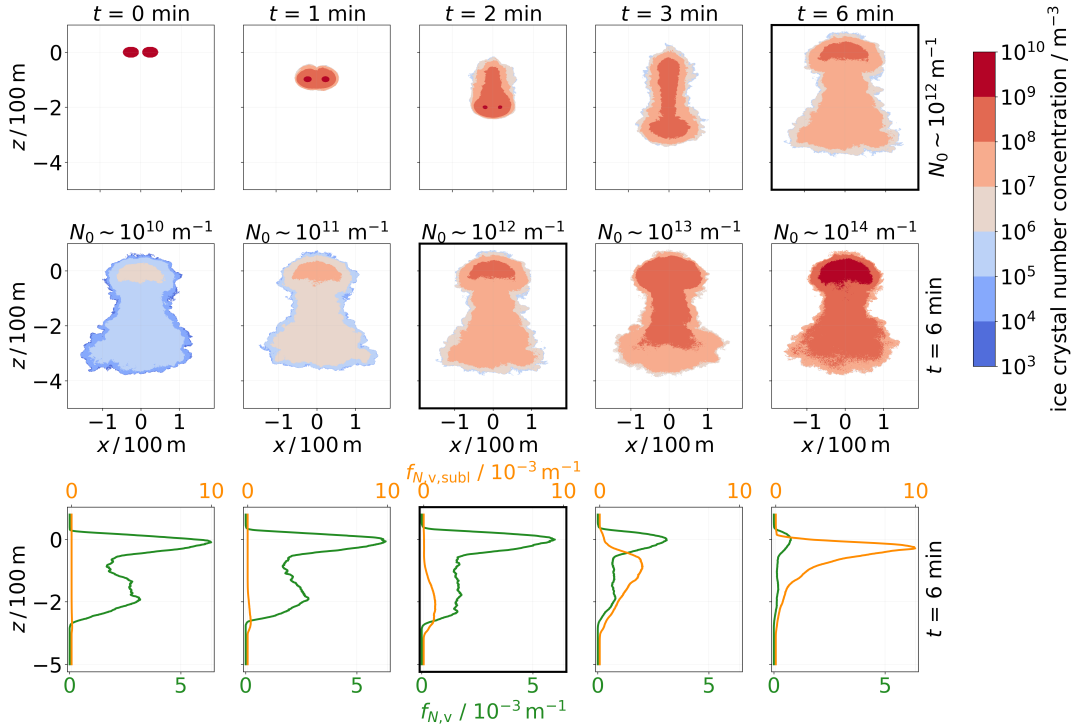
Figure 2. Ice crystal number concentrations, averaged along the flight direction in the x, z-plane, are depicted in the first and second rows. The first row illustrates the temporal evolution over six minutes. The final concentration distribution is displayed in the second row for five different N_0 values. The third row shows the normalized vertical profiles of ice crystals (green) and sublimated ice crystals (orange) (the first row depicts one simulation, and the second and third rows depict five different simulations). The simulation displayed in the top row refers to the simulation in the middle panels in the second and third rows, marked by the black frame. The displayed simulations are performed for an A350 aircraft at $T_{CA} = 217\,\mathrm{K}$, $RH_{i,amb} = 120\,\%$, and $I_0 = I_{0,H_2}$. The z-coordinate is shifted such that $z = 0\,\mathrm{m}$ corresponds to the cruise altitude (which is also done in Figs. 4, 5, and 6).
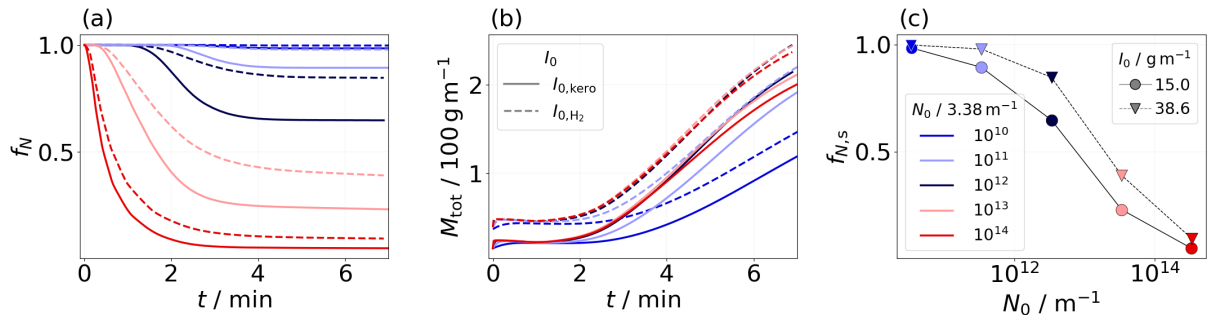

Figure 3. Temporal evolution of the normalized total number of ice crystals and total ice mass for different values of N_0 and I_0 ((a) and (b)). In panel (c), the survival fractions as functions of N_0 are depicted.

concentration at higher temperatures, they experience, in absolute terms, a stronger increase of the saturation pressure within the descending vortices, leading to increased sublimation (Unterstrasser, 2016; Bier and Burkhardt, 2022). This phenomenon is most pronounced in the N_0-upscaling cases.

The sensitivity of the survival fraction to the ambient relative humidity and ambient temperature is illustrated in the bottom row (3). In addition to the default cases with $I_0 = I_{0,H_2}$, data points for the kerosene reference case with $I_0 = I_{0,\text{kero}}$ are displayed for $T_{CA} = 217\,\text{K}$ and $225\,\text{K}$ (yellow symbols). Simulations with $I_0 = I_{0,H_2}$ indicate that ice crystals, which would typically sublimate under $I_{0,\text{kero}}$ conditions, are now sufficiently large to withstand adiabatic heating. This effect is most pronounced in the $RH_{i,\text{amb}} = 110\,\%$, N_0-downscaling scenarios (the differences between the yellow and the colored squares are larger than the differences between the yellow and colored circles at $N_0 \lesssim 10^{13}\,\text{m}^{-1}$). Simulations at a lower ambient relative humidity (squared symbols) show a stronger loss of ice crystals, a trend consistent across the variations regarding N_0 and I_0. This is due to the stronger sublimation effects in the primary wake in case of a reduced relative humidity value (Unterstrasser et al., 2014; Unterstrasser, 2016). Notably, in the extreme N_0-downscaling scenario ($N_0 \sim 10^{10}\,\text{m}^{-1}$) at $120\,\%$ relative humidity, the survival fraction remains largely unaffected by the ambient temperature, with survival fractions equal or close to one at both $217\,\text{K}$ ($f_{N,s} = 1.00$) and $235\,\text{K}$ ($f_{N,s} = 0.95$). In contrast, for the extreme N_0-upscaling scenario, the impact of ambient temperature is significantly more pronounced, reducing the survival fraction by a factor of 4.5, from $f_{N,s} = 0.09$ at $217\,\text{K}$ down to $f_{N,s} = 0.02$ at $235\,\text{K}$. This temperature sensitivity is further amplified in drier atmospheric conditions, where the effect on the survival fraction is more substantial. For the N_0-downscaling scenario, the survival fraction decreases by a factor of 2.24, while in the N_0-upscaling case, the reduction exceeds even one order of magnitude. In the upscaling cases with ambient temperatures at or above $230\,\text{K}$, nearly all ice crystals sublimate, with $f_{N,s} < 0.15$. Initial differences in N_0 spanning four orders of magnitude are reduced to 2.98 ($217\,\text{K}$, $120\,\%$) and 2.85 ($217\,\text{K}$, $110\,\%$), and further decrease to 2.37 ($235\,\text{K}$, $120\,\%$) and 2.14 ($235\,\text{K}$, $110\,\%$), highlighting the importance of both parameters in the context of ice crystal loss during the vortex phase.

The third ambient parameter varied in this study is stratification. Following e.g. Unterstrasser et al. (2014), we use a Brunt-Väisälä frequency of $N_{BV} = 1.15 \times 10^{-2}\,\text{s}^{-1}$ as the default, and a smaller value, $N_{BV} = 0.5 \times 10^{-2}\,\text{s}^{-1}$, which characterizes an atmosphere with weaker atmospheric stability. The simulation domain needs to be larger in the latter case as the downward movement and oscillation of the vortex system are stronger. Therefore, to reduce the number of simulations and associated computational costs, we varied N_0 only by a factor of 100 (both up and down). This simulation set is performed only for $T_{CA} = 217\,\text{K}$.

Figure 5 displays normalized vertical profiles of the final ice crystal number (panel (a)) and number of sublimated ice crystals (panel (b)) for both stratification scenarios (indicated by linestyle). Only simulations with $I_0 = I_{0,H_2}$ are displayed here. Evidently, in a weakly stratified ambient atmosphere, the wake vortices generally descend further down. Consequently, sublimation extends to lower altitudes (especially in the default and N_0-downscaling cases, displayed by the black and blue curves). This is mainly observed in the simulations with default or lower N_0 value as the difference in the final contrail height is about $200\,\text{m}$, compared to about $50\,\text{m}$ in the N_0-upscaling scenario. This reduced difference in the N_0-upscaling case is because most ice crystals are lost at higher altitudes, independently of stratification. As anticipated, the survival fraction is
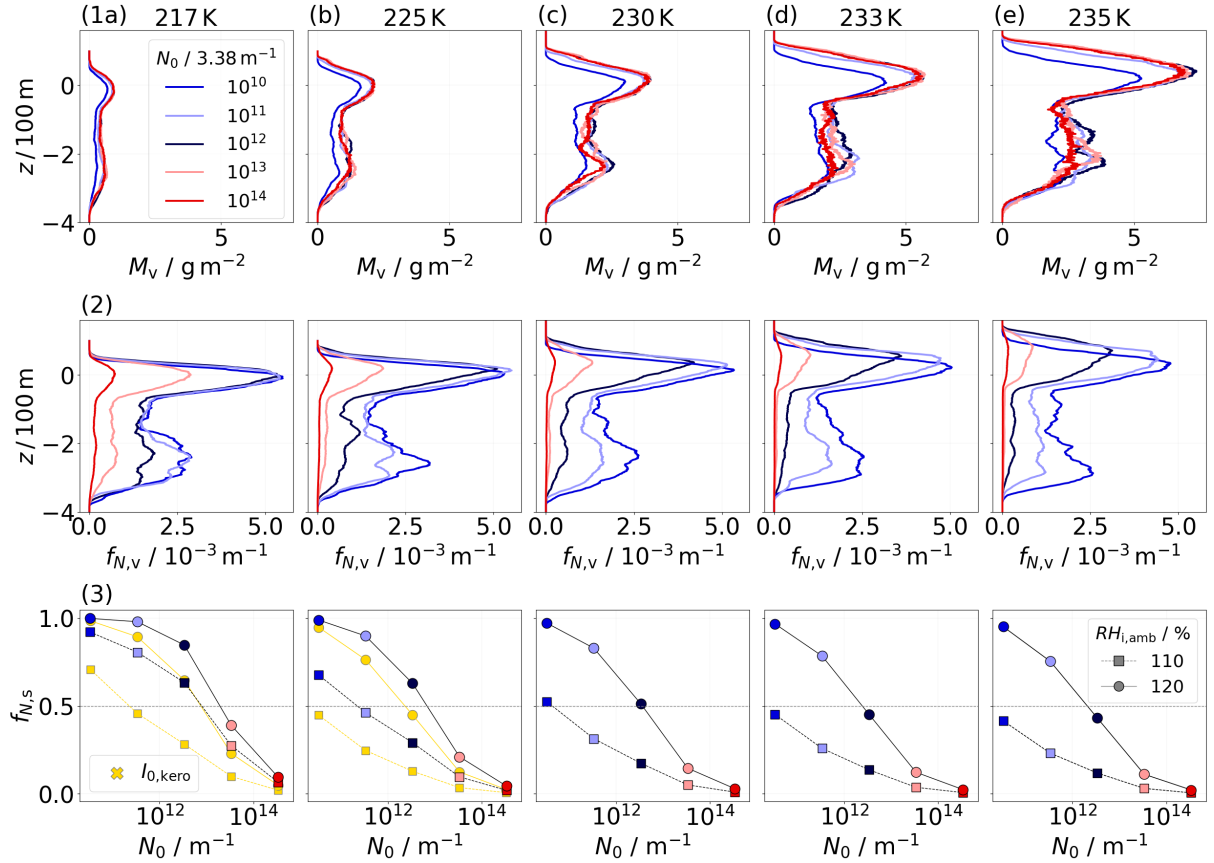
Figure 4. Final vertical profiles of ice mass (first row) and normalized ice crystal number (second row) for different N_0 values (as given in the legend in panel (1a)) after six minutes. Columns depict results for ambient temperatures of 217 K, 225 K, 230 K, 233 K, and 235 K (see titles on top). The ambient relative humidity is 120 %. The third row displays the survival fraction at the two different humidity values as indicated in panel (3e). At $T_{CA} = 217$ K and 225 K, yellow symbols, which refer to simulations with $I_0 = I_{0,\text{kero}}$, are plotted for comparison. A horizontal dashed line at $f_{N,s} = 0.5$ is provided as a visual guide.

reduced for contrails evolving in a weakly stratified atmosphere. Decreasing the ambient relative humidity exacerbates crystal
305   loss further. Also, lower survival fractions are observed in scenarios with $I_0 = I_{0,\text{kero}}$, as previously noted (not shown). The original four orders of magnitude difference in N_0 decreases to 2.69 and 2.46 (default and weakly stratified, 120 %), and 2.46 and 2.31 (110 %) at $I_0 = I_{0,\text{kero}}$, as well as 2.98 and 2.72 (120 %), and 2.85 and 2.66 (110 %) at $I_0 = I_{0,\text{H}_2}$.

3.2.2   Sensitivity to the microphysical initialization

We prescribe the initial ice crystal size distribution (SD) as a lognormal distribution with a specified width parameter r_{SD},
310   see e.g. Unterstrasser and Sölch (2010). A variation of r_{SD} has been shown to have a non-negligible effect on the contrail's
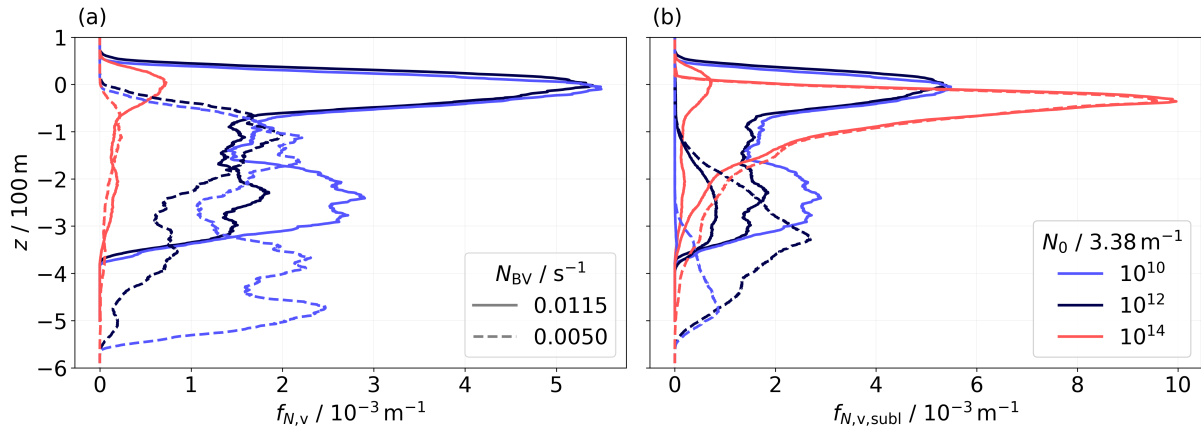
Figure 5. Final vertical profiles of normalized number of ice crystals (panel (a)) and normalized number of sublimated ice crystals (panel (b)). Results for default (solid lines) and weaker (dashed lines) atmospheric stability are depicted. The displayed simulation results correspond to $T_{CA} = 217\,K$, $RH_{i,amb} = 120\%$, and $I_0 = I_{0,H_2}$.
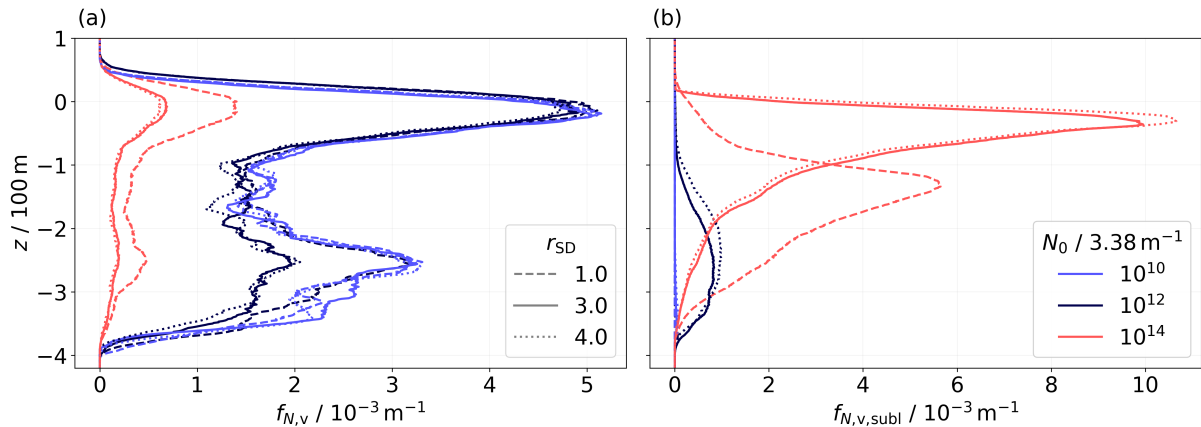

Figure 6. Final vertical profiles of normalized number of ice crystals (panel (a)) and normalized number of sublimated ice crystals (panel (b)). Solid lines represent the reference cases with $r_{SD} = 3.0$, while initially broader and narrower size distributions are depicted by dotted and dashed lines, respectively. The shown simulations were conducted for $T_{CA} = 217\,K$, $RH_{i,amb} = 120\%$, and $I_0 = I_{0,H_2}$.

evolution during the vortex phase (Unterstrasser, 2014). Varying the width, we adjust the geometric mean diameter such that the total initial ice mass and ice crystal number are unaffected (Unterstrasser, 2014).

In Fig. 6, we present simulations, where r_{SD} is varied according to Tab. 1. The final contrail height for each N_0 scenario appears relatively unaffected by variations in r_{SD}, as shown in Fig. 6(a). However, a narrower initial SD leads to a higher number of ice crystals present at lower altitudes (dashed curves). This can be explained by the delayed onset of sublimation, which occurs at lower altitudes (see panel (b)). In contrast, a broader initial SD results in a higher proportion of smaller ice crystals at
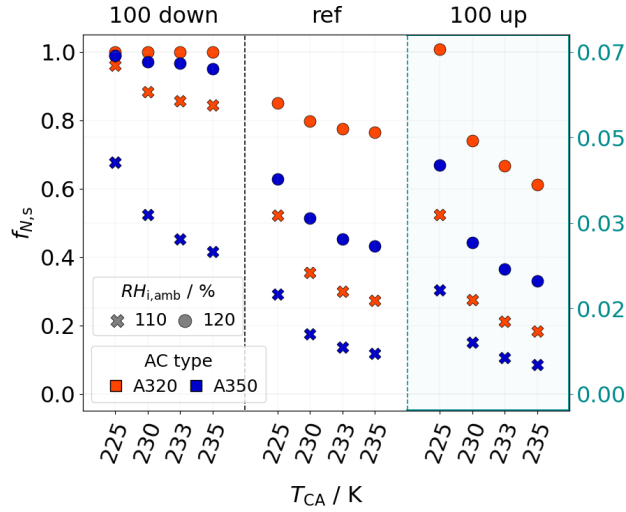
315

Figure 7. Survival fractions of an A320 (red) and an A350 (blue) aircraft. The three boxes represent the ice crystal number scaling as indicated in the title, where e.g. "100 down" refers to the simulation with N_0 equal to $3.38 \times 10^{10}\,\mathrm{m}^{-1}$ (A350) or $0.85 \times 10^{10}\,\mathrm{m}^{-1}$ (A320). In the case of a factor 100 upscaling, the survival fractions are small. Hence, we adapted the axis as indicated by the light blue labels. Simulation results for both values of ambient relative humidity are shown (symbol).

the start, which tend to sublimate at higher altitudes, leading to lower survival fractions. This pattern is observed consistently across all N_0 scenarios. To assess the robustness of these results with respect to ambient temperature, we repeated this set of simulations at $T_{\mathrm{CA}} = 233\,\mathrm{K}$. The general trends related to r_{SD} remain unchanged by the variation in ambient temperature.

320 However, as expected based on previous findings, we observe lower survival fractions at this temperature.

In aircraft plumes characterized by negligible soot emission, such as those from hydrogen-powered engines, ice nucleation is assumed to predominantly occur on entrained ambient aerosol particles (Bier et al., 2024). The dry radii of these ambient aerosols, therefore, govern the size of the resulting ice crystals. Bier et al. (2024) identified several aerosol modes with sizes spanning from few nanometers to several micrometers. This broad size range is more accurately captured by an initial size

325 distribution with larger values of r_{SD} (e.g. 3.0 and 4.0), thus considered more representative of the physical conditions.

3.2.3 Sensitivity to aircraft type

H$_2$-contrail simulations for a smaller A320 aircraft with a wing span of $b_{\mathrm{span}} = 34.4\,\mathrm{m}$ are performed for $T_{\mathrm{CA}} \geq 225\,\mathrm{K}$. The grid spacing is adapted as outlined in Tab. 1. We simulate this aircraft type only with a N_0-scaling factor of 100.

Unterstrasser and Görsch (2014) have done baseline simulations for an A320 aircraft in typical kerosene conditions. As

330 revealed in this study, the altitude where sublimation starts is independent of the aircraft type. As described in Sec. 2.2, both N_0 and I_0 are linearly dependent on the fuel flow rate. Since $\mathrm{EI}_{\mathrm{iceno}}$ and $\mathrm{EI}_{\mathrm{H_2O}}$ are assumed to be constant across all aircraft types, the mean mass and radius of the initial ice crystals are consequently independent of the aircraft type, as both are proportional to
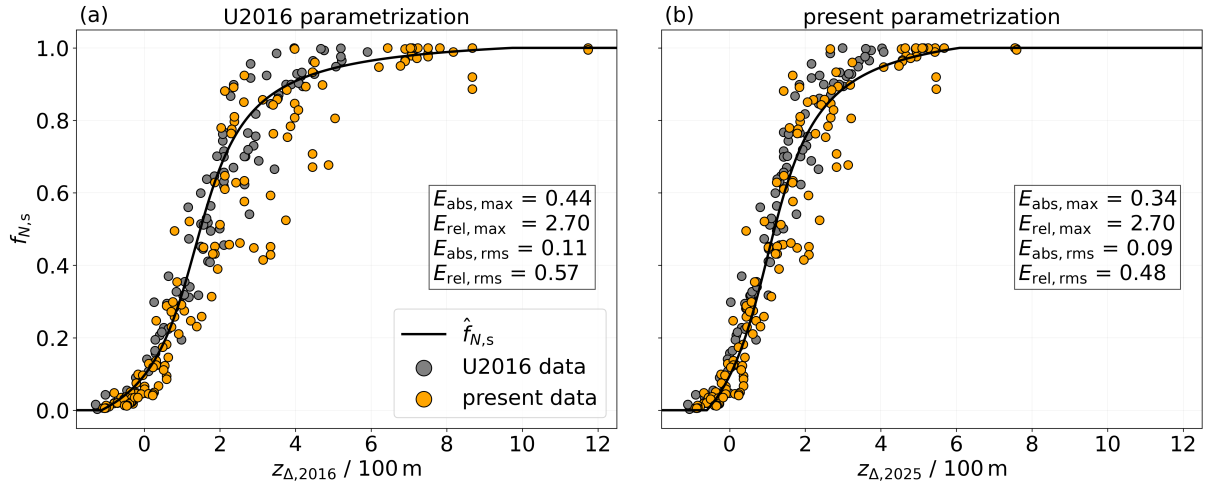
Figure 8. Simulated survival fraction as a function of the parameter z_Δ. The original (a) and updated (b) parametrizations are denoted by the solid black line. Grey points represent the simulated survival fractions from the 2016 study, while orange points correspond to those from the present study. Since the fit coefficients are adapted in the new formulation, the z_Δ parameter differs in both versions, denoted by $z_{\Delta,2016}$ and $z_{\Delta,2025}$.

the ratio I_0/N_0. However, the vortex system of the A320 descends more slowly. Therefore, the sublimation threshold altitude is reached later. The vortices of the A320 dissolve before such low altitudes can be reached, where strong sublimation occurs.

335 This decreases sublimation effects in the primary wake, allowing more ice crystals to survive the vortex phase for smaller aircraft like the A320 than larger ones like the A350. This trend holds across all N_0-scaling scenarios. Although the final A350 contrail still contains more ice crystals than the A320 contrail, the relative ice crystal loss is greater for the A350, reducing the initial large differences in ice crystal numbers.

Figure 7 shows how the survival fractions depend on the aircraft type. Each box, delineated by the dashed vertical lines,

340 corresponds to a different N_0-scaling scenario. Note that in the factor 100 upscaling scenario, where the survival fractions are less than 0.1, the y-axis is adjusted accordingly. For each scenario, simulations at $T_{CA} = 225\,\text{K}$, $230\,\text{K}$, $233\,\text{K}$, and $235\,\text{K}$ are performed, as indicated on the x-axis. As discussed in Sec. 3.2.1, high ambient temperatures and low relative humidity increase ice crystal loss. Overall, the A320 exhibits higher survival fractions, with the most pronounced differences at low N_0 values and low ambient humidity (e.g. $f_{N,s} = 0.84$ for the A320 and $f_{N,s} = 0.42$ for the A350 at $T_{CA} = 235\,\text{K}$). In scenarios with a

345 strong N_0 upscaling, nearly all ice crystals sublimate regardless of aircraft type ($f_{N,s} \leq 0.07$).

3.3 Parametrization of ice crystal loss

Unterstrasser (2016, from now on U2016) presents an ice crystal loss parametrization that approximates the survival fraction of ice crystals after the vortex phase $f_{N,s}$ and takes into account the impact of ambient relative humidity, temperature at cruise altitude, thermal stratification, apparent ice crystal emission index, and aircraft parameters. Relevant aircraft parameters are

350　the water vapor emission I_0, the wing span b_{span}, and the wake vortices' initial circulation Γ_0. A typical application of the parametrization is the implementation in larger scale contrail models where the contrail initialization refers to some state after vortex break-up, and effects of the wake dynamics cannot be explicitly resolved. The development of the parametrization was based on a database of > 80 EULAG-LCM simulations, which are sensitivity studies with variations of the parameters above. Notably, the focus at that time was on contrails from kerosene combustion. The new set of H_2-contrail simulations investigates

355　the sensitivity to N_0 more systematically and over a broader range. Moreover, contrails at temperatures above 225 K have not been considered previously, and the validity of the parametrization beyond this temperature threshold is not guaranteed.

　　The following paragraphs will briefly repeat the parametrization formulation, describe appropriate adaptations, and analyze its applicability and performance for the new H_2-contrail data set.

　　The ice crystal loss during the vortex phase can be assessed by introducing three length scales that describe the processes

360　relevant to downward propagating contrail ice crystals.

- – z_{desc} is the final vertical displacement of the wake vortex system, which leads to a maximum adiabatic heating experienced in the primary wake. The quantity depends most strongly on thermal stratification, aircraft mass, and wingspan.

- – z_{atm} measures the effect of the ambient supersaturation on the ice crystal mass budget. z_{atm} is the distance an air parcel has to travel down until its saturation pressure equals its vapor pressure (i.e. until its supersaturation is depleted due to

365　adiabatic heating). The quantity depends most strongly on the ambient relative humidity.

- – z_{emit} measures the effect of the water vapor emission on the ice crystal mass budget. Analogously to z_{atm}, z_{emit} corresponds to an adiabatic heating such that an initially saturated parcel remains at saturation when the emitted water vapor is added to the parcel. The quantity depends on the ambient temperature and the amount of emitted water vapor, which in turn depends on the fuel consumption, the emission index of water vapor, and the contrail cross-section.

370　The exact definitions of these length scales are given in Sec. 3.1 of U2016. We repeat the definition of z_{desc}, which is given by

$$z_{\mathrm{desc}} = \left(\frac{8\,\Gamma_0}{\pi\,N_{\mathrm{BV}}} \right)^{1/2}. \tag{6}$$

Regarding z_{atm} and z_{emit}, we implement slightly redefined formulae. In the previous version, the definitions of z_{atm} and z_{emit} are based on the assumption of balancing water vapor concentrations. In the updated parametrization, we redefine the two length

375　scales by requiring the conservation of water vapor mass mixing ratios, which are the quantities that are actually conserved under adiabatic changes. Hence, we introduce the adiabatic index $\kappa = 3.5$, and the modified equations read as

$$(1 + s_{\mathrm{i}})\, \frac{e_{\mathrm{s}}(T_{\mathrm{CA}})}{T_{\mathrm{CA}}{}^{\kappa}} = \frac{e_{\mathrm{s}}(T_{\mathrm{CA}} + \Gamma_{\mathrm{d}}\, z_{\mathrm{atm}})}{(T_{\mathrm{CA}} + \Gamma_{\mathrm{d}}\, z_{\mathrm{atm}})^{\kappa}} \tag{7}$$

and

$$\frac{e_{\mathrm{s}}(T_{\mathrm{CA}})}{R_{\mathrm{WV}}\, T_{\mathrm{CA}}{}^{\kappa}} + \frac{\rho_{\mathrm{emit}}}{T_{\mathrm{CA}}{}^{\kappa-1}} = \frac{e_{\mathrm{s}}(T_{\mathrm{CA}} + \Gamma_{\mathrm{d}}\, z_{\mathrm{emit}})}{R_{\mathrm{WV}}\, (T_{\mathrm{CA}} + \Gamma_{\mathrm{d}}\, z_{\mathrm{emit}})^{\kappa}}. \tag{8}$$

380   Γ_d is the dry adiabatic lapse rate, with a value of $9.8\,\mathrm{K\,km^{-1}}$. The water vapor saturation pressure is represented by e_s, and $s_i = RH_i - 1$ denotes the supersaturation. According to U2016, we then define a linear combination of these length scales

$$z_\Delta = \tilde{\alpha}_{\mathrm{atm}}\, z_{\mathrm{atm}} + \tilde{\alpha}_{\mathrm{emit}}\, z_{\mathrm{emit}} - \tilde{\alpha}_{\mathrm{desc}}\, \hat{z}_{\mathrm{desc}} \qquad (9)$$

with positive weights $\tilde{\alpha}_X$.

    z_Δ is large if the buffer effect of the ambient supersaturation and the emitted water vapor outweighs the adiabatic heating

385 due to the wake vortex descent. This means, the water vapor surplus is sufficient to keep the heated air parcel supersaturated. [*Side remark: Note that in the simulations, the air parcel does not remain supersaturated, but RH_i quickly relaxes to 100 %. Figure 3b reveals that the water vapor surplus deposits on the ice crystals within a few seconds (for large N_0) or within at most 30 s (for low N_0). The local maximum attained within the first half a minute clearly relates to the water vapor surplus as estimated by the two length scales z_{atm} and z_{emit}. Note that the increase in ice mass after two minutes is due to detrained*

390 *ice crystals outside of the vortex system, which grow in the supersaturated ambient air. Figure 2a in Unterstrasser and Sölch (2010) displays the evolution of the total ice mass in the descending wake vortex system. This nicely reveals the dependence of the peak value on the water vapor surplus and the subsequent monotonic decrease of the ice mass. Hence, the buffer effect is achieved by increasing the total mass and the mass concentrations of the ice crystals in the vortex system. The larger those quantities are after the initial growth period, the more and the longer the ice crystals can shrink until complete sublimation.*]

395   A small z_Δ (including also negative values) means that the wake vortex descent prevails for so long that a substantial fraction or even all the entrained ice crystals are likely lost.

    Following U2016, both $\tilde{\alpha}_{\mathrm{atm}}$ and $\tilde{\alpha}_{\mathrm{emit}}$ are modified to include the effect of a variation of N_0, while $\tilde{\alpha}_{\mathrm{desc}}$ can be left unchanged (i.e. $\alpha_{\mathrm{desc}} = \tilde{\alpha}_{\mathrm{desc}}$):

$$z_\Delta = \Psi^\gamma (\alpha_{\mathrm{atm}}\, z_{\mathrm{atm}} + \alpha_{\mathrm{emit}}\, z_{\mathrm{emit}}) - \alpha_{\mathrm{desc}}\, \hat{z}_{\mathrm{desc}}. \qquad (10)$$

400 In U2016, Ψ was given by $\frac{1}{\mathrm{EI}^*_{\mathrm{iceno}}}$ with $\mathrm{EI}^*_{\mathrm{iceno}} = \frac{\mathrm{EI}_{\mathrm{iceno}}}{\mathrm{EI}_{\mathrm{iceno,ref}}}$ and a positive constant γ. In the new formulation, Ψ is defined as

$$\Psi = 1/n_0^*, \qquad (11)$$

where n_0 is an (intermediate) ice crystal number concentration and the starred quantity is the value normalized by a reference value $n_{0,\mathrm{ref}}$. In both approaches, increasing $\mathrm{EI}_{\mathrm{iceno}}$ (in the original formulation) or n_0 (in the new formulation) gives smaller weights $\tilde{\alpha}_{\mathrm{atm}}$ and $\tilde{\alpha}_{\mathrm{emit}}$. This reduces the buffer effect and, consequently, z_Δ. This reflects the fact that ice crystal loss becomes

405 more substantial when the water vapor surplus is distributed over more ice crystals with smaller masses on average. With smaller mean ice crystal sizes, a specific fraction of lost ice mass translates into a larger relative fraction of lost ice crystals.

    The definition of n_0 is deferred to the Appendix (Eq. (A1)) and the motivation for the switch from $\mathrm{EI}^*_{\mathrm{iceno}}$ to n_0^* is explained in Sec. 4.

    The three length scales depend only on input parameters and can be evaluated for given meteorological and aircraft proper-

410 ties. Notably, they are independent of N_0, and the sensitivity of z_Δ to N_0 enters the parametrization solely by an adaptation of the weights $\tilde{\alpha}_{\mathrm{atm}}$ and $\tilde{\alpha}_{\mathrm{emit}}$.

Plotting the simulated $f_{N,s}$ values as functions of z_Δ with suitably chosen weights, the data points can be reasonably well approximated by an arc tangent function. Hence, the parametrized survival fraction $\hat{f}_{N,s}$ can then be defined as

$$\hat{f}_{N,s} = \hat{a}(z_\Delta), \tag{12}$$

with

$$\hat{a}(x) = \beta_0 + \frac{\beta_1}{\pi} \arctan\left(\alpha_0 + (x/100\,\mathrm{m})\right). \tag{13}$$

In the following, we outline our procedure for determining the new set of fit coefficients. Simulations with $r_{SD} = 1.0$ and $r_{SD} = 4.0$, accounting for approximately $25\,\%$ of the total dataset, were excluded from the fitting process, as they represent extreme cases of the size distribution width. However, these simulations are still shown in Fig. 8. We selected a representative subset of simulations using the default value of $r_{SD} = 3.0$. Additionally, some data points from simulations with weaker stability were identified as outliers and excluded. Consequently, $69\,\%$ of the new simulations and the entire data set from U2016 were used to derive the fit coefficients. A weighting was applied in the fitting procedure, with all data points at $RH_{i,amb} = 110\,\%$ and $EI^*_{iceno} > 1$ being assigned higher weights (1.1 and 2.0, respectively). On the one hand, these weights were introduced to reduce the absolute errors of the $RH_{i,amb} = 110\,\%$ cases. This is favorable as the survival fractions are systematically smaller than for the $RH_{i,amb} = 120\,\%$ cases. Hence, similar absolute errors over both sets of simulations would imply larger relative errors for $RH_{i,amb} = 110\,\%$ cases. Furthermore, the occurrence frequency of ice supersaturation is exponentially distributed with decreasing encounter probabilities for increasing $RH_{i,amb}$ values (Petzold et al., 2017). Increasing the weights is a pragmatic solution to put more emphasis on the low-$RH_{i,amb}$ cases.

We propose the following values for the fitting coefficients:

$$\beta_0 = 0.42, \tag{14a}$$

$$\beta_1 = 1.31, \tag{14b}$$

$$\alpha_0 = -1.00, \tag{14c}$$

$$\alpha_{atm} = 1.27, \tag{14d}$$

$$\alpha_{emit} = 0.42, \tag{14e}$$

$$\alpha_{desc} = 0.49, \tag{14f}$$

$$\gamma = 0.16. \tag{14g}$$

Figure 8 presents a comparison between both versions, where the simulation data used to derive the original parametrization formulation are displayed in grey, and the present (additional) data points are shown in orange. Panel (a) depicts the 2016 parametrization curve. The new parametrization (panel (b)) reduces both the absolute maximum and root mean square error (see values inserted in the figure). The absolute root mean square is reduced by $2\,\%$, whereas the relative root mean square error of the U2016 data is decreased by $9\,\%$. Relative to the U2016 database, the new H_2 simulations sample particularly the
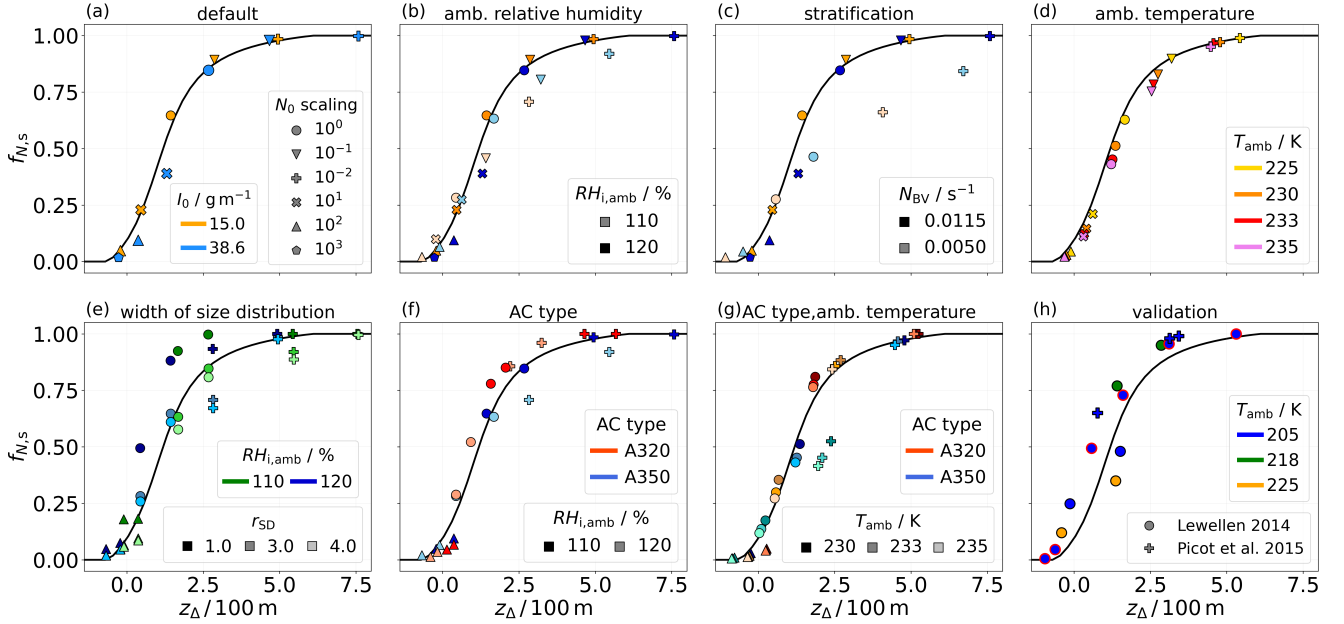
Figure 9. Simulated survival fractions as functions of the parameter z_Δ ($= z_{\Delta,2025}$), focusing exclusively on new H_2 simulations. The symbol legend in panel (a) applies to the panels (a)-(g), with symbols indicating N_0-scaling information. In panels (a)-(c), blue symbols denote hydrogen water vapor emissions, while orange symbols represent kerosene cases. Each panel highlights a different meteorological or aircraft scenario, as the titles indicate. Panel (h) displays survival fractions from other studies for comparison and validation. There, symbols with a red outline correspond to a study investigating the effects of varying the ice crystal emission index (Lewellen et al., 2014).

space for large and very small $f_{N,s}$ values more densely. The supplement contains further plots that help to rate the changes implied by the new version.

In Fig. 9, we show the updated parametrization for various meteorological and aircraft scenarios. As indicated by its title,
445   each panel highlights specific sensitivity analyses. The dependencies of the survival rate on the input parameters have been thoroughly explained in the preceding sections. The following will discuss the new insights gained from the updated parametrization. It can be observed that simulations performed at temperatures above 225 K are well represented by the parametrization. This holds for both the N_0-upscaling and -downscaling scenarios. While a critical temperature exists above which contrail formation is not possible, this temperature threshold has no direct relevance for the microphysical processes during the vortex
450   phase. Hence, it is not surprising that the validity of the parametrization extends beyond 225 K.

The parametrization does not account for variations in r_{SD}, meaning that data points from simulations with different r_{SD} values but the same z_Δ value are treated identically. Notably, for N_0-upscaling cases, simulations with $r_{SD} = 1.0$ tend to show survival fractions that are somewhat overestimated. For the time being, this is an irreducible uncertainty partly due to idealizations in our initialization.

455   Regarding aircraft type, the parametrization effectively represents both A350 (bluish) and A320 (reddish) cases across upscaling and downscaling scenarios, as shown in panels (f) and (g). Additionally, the parametrization is consistent with other simulation results from studies such as Lewellen et al. (2014) and Picot et al. (2015), as highlighted in panel (h). Our updated H_2 parametrization not only aligns well with these results, but also particularly captures the ice crystal emission index variation study from Lewellen (2014), further demonstrating the validity of the new parametrization.

460 ### 3.4   Impact of vortex phase processes on contrail-cirrus evolution

This section presents results of contrail-cirrus simulations and demonstrates the relevance of the ice crystal number in young contrails for the subsequent transition into contrail-cirrus.

    We employ the EULAG-LCM model in a setup largely based on that used in Unterstrasser et al. (2017a) and Unterstrasser et al. (2017b). We use a domain with two dimensions, x (horizontal) and z (vertical), that is perpendicular to the direction of
465 flight. We embed the data of the vortex phase simulation (averaged along the flight direction) in a significantly larger simulation domain spanning $40\,\mathrm{km}$ in x- and $2.5\,\mathrm{km}$ in z-direction, with grid resolutions of $\mathrm{d}x = \mathrm{d}z = 10\,\mathrm{m}$. The simulated time is $8\,\mathrm{h}$. The sedimentation velocities are determined using the Reynolds number and the maximum particle dimensions, as described in the Appendix of Sölch and Kärcher (2010). We prescribe a stepwise vertical profile of relative humidity, assuming an ambient ice supersaturated layer of $120\,\%$ between 1 and $2\,\mathrm{km}$ (see further details in, e.g., Unterstrasser et al. (2017a)). We also impose
470 a synoptic-scale updraught (with an updraught velocity $w = 1\,\mathrm{cm\,s^{-1}}$) over roughly six hours, leading to a final adiabatic cooling of $2\,\mathrm{K}$. We choose an A350 aircraft with $T_{\mathrm{CA}} = 225\,\mathrm{K}$, $N_{\mathrm{BV}} = 1.15 \times 10^{-2}\,\mathrm{s^{-1}}$, $I_0 = I_{0,\mathrm{H_2}}$, and $r_{\mathrm{SD}} = 3.0$. In the first simulation series, the contrail-cirrus initialization is directly based on the results from the according vortex phase simulation. The initialized contrail consists of $N = f_{N,\mathrm{s}} \times N_0$ ice crystals. In the second simulation series, we deliberately disregard vortex phase loss processes and initialize a contrail with N_0 ice crystals. This is accomplished by using the contrail data from the first
475 simulation series and uniformly scaling up the ice crystal number concentrations by a factor of $(f_{N,\mathrm{s}})^{-1}$.

    An important quantity for analyzing contrail evolution is the total extinction, which serves as a metric for the radiative effect of an individual contrail (Unterstrasser, 2020). It is defined as the horizontal integral of the extinction, $1 - \exp(-\tau)$, where τ represents the optical thickness along the vertical direction. Then, total extinction is expressed as:

$$
\begin{aligned}
E(t) &= \int (1 - \exp(-\tau(x,t)))\,\mathrm{d}x \approx \int \tau(x,t)\,\mathrm{d}x \\
&= \iint \chi(x,z,t)\,\mathrm{d}z\,\mathrm{d}x,
\end{aligned}
\tag{15}
$$

480 where $\chi(x,z,t)$ is the extinction coefficient. It is proportional to the projected area of the ice crystals per unit volume. We assume an extinction efficiency $Q_{\mathrm{ext}} = 2$, as described in Schumann et al. (2011). Figure 10 illustrates the temporal evolution of the total ice crystal number (panel (a)) and the total extinction (panel (b)). In both panels, the color represents the N_0 scaling, with red indicating upscaling scenarios and blue denoting downscaling scenarios. The line style differentiates between the two setups.

485   Three key observations emerge: Firstly, E is significantly higher in the N_0-upscaled scenarios. This outcome is expected, as total extinction is proportional to the effective surface area of the ice crystals; a larger number of ice crystals, as shown in panel
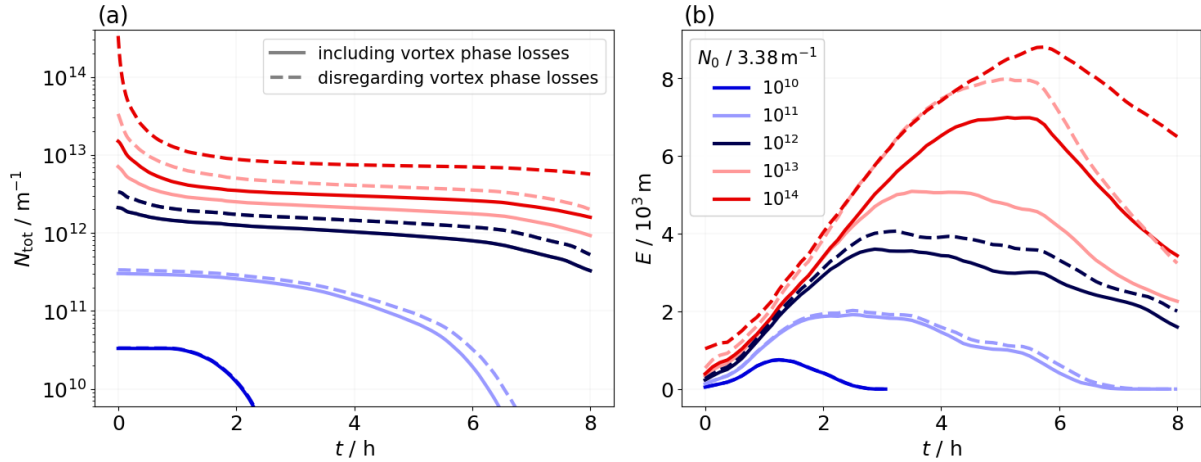
Figure 10. Time evolution of the total number of ice crystals (a) and total extinction (b) for the N_0-up- and downscaling cases. In the first simulation series, the contrails are initialized by using the final state from the respective vortex phase simulations; in the second simulation series, the ice crystal numbers are upscaled by the respective survival fractions.

(a), leads to a greater extinction. Secondly, the contrail(-cirrus) dissipates more quickly when N_0 is smaller. In the scenario where N_0 is reduced by a factor of 100 (dark blue), the contrail disappears after only few hours, indicating a significantly shorter lifetime. Thirdly, we observe an increase in E in the scenarios where the vortex phase losses are disregarded. In these cases, the contrail is initialized with more ice crystals compared to the first simulation series (see panel (a)).

A qualitative comparison of the two setups can be made by examining the lifetime-integrated total extinction values, $\hat{E} = \int E(t)\,\mathrm{d}t$, that are displayed in Fig. 11(a). Ignoring vortex phase losses leads, at maximum, to a difference in lifetime-integrated total extinction of 46%. This indicates that the radiative impact of an individual contrail can be significantly overestimated if vortex phase processes, such as contrail expansion and ice crystal sublimation in the primary wake, are not considered. The nonlinear increase in the $\hat{E}$ difference between both setups in the N_0-upscaled simulations may be attributed to saturation effects. As the number of ice crystals increases, competition for available water vapor in the spreading contrail-cirrus becomes more important. Consequently, the peak ice mass does not continue to grow indefinitely with increasing N_0 values but is expected to reach a limit eventually. This explains why the simulation with a 100-fold increase in N_0 shows a smaller increase in lifetime-integrated total extinction when disregarding the vortex phase losses compared to the simulation with a 10-fold increase in N_0. We repeated this kind of simulation series, i.e. disregarding the crystal losses from the vortex phase, for the $I_{0,\mathrm{kero}}$ scenario. Interestingly, we observe only a small impact on the lifetime-integrated total extinction when the vortex phase losses are ignored (see Fig. 11(b)). This suggests that the initial water vapor emission, compared to the ice crystal number, has only a minor impact on the radiative effect of a single contrail-cirrus.

This is just one example of a contrail-cirrus simulation set. A comprehensive analysis, examining various meteorological parameters, will follow.
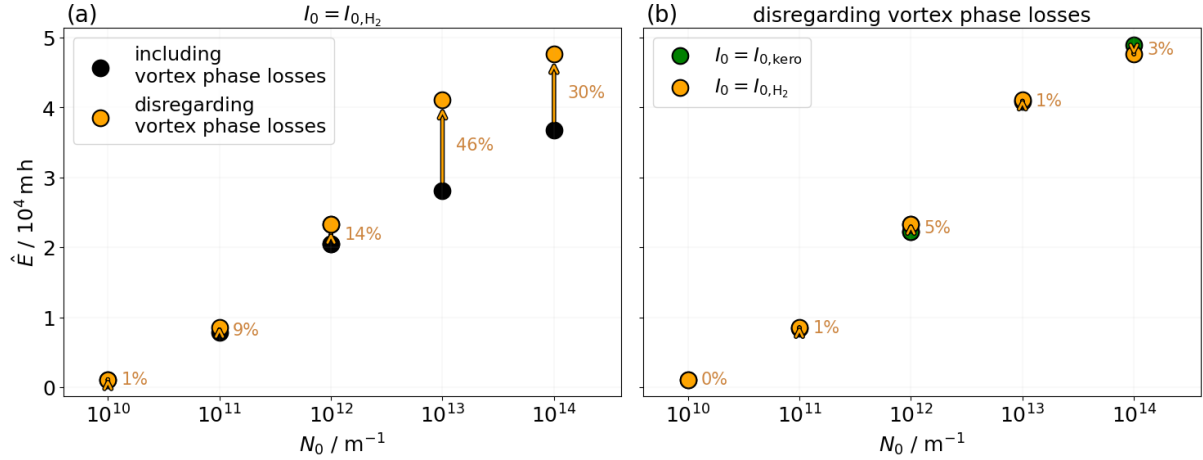
Figure 11. Lifetime-integrated total extinction $\hat{E}$ for all five N_0-scaling scenarios. Panel (a) highlights the increase of this quantity in the second simulation series (shown by the orange points). Panel (b) displays $\hat{E}$ for both I_0 options. The orange points are the same in both panels.

4 Discussion

This study highlights the importance of ice crystal loss during the vortex phase depending on the propulsion system. While previous research has examined the effect of initial ice crystal numbers on crystal loss — such as Lewellen (2014), who varied the ice crystal emission index across six orders of magnitude, and Unterstrasser (2014), who explored a variation over two orders of magnitude — this work takes a systematic approach tailored explicitly to H_2 contrails. It uniquely combines variations in the initial number of ice crystals with adjustments to the emitted water vapor mass. The N_0-upscaling scenarios may not only represent a potential H_2 fuel cell setup but also account for the formation of contrail ice crystals on ultrafine volatile particles (UFPs). UFPs, typically nm-sized particles, can contribute to ice crystal formation if the plume supersaturation is high enough to overcome the Kelvin barrier for activation (Kärcher et al., 2015). This requires the reduction of the soot particle number at least 10-fold, preventing them from acting as the primary condensation nuclei for water vapor, and an ambient temperature significantly below the formation threshold (Kärcher, 2018).

In addition to nitrogen species emissions from H_2 engines, oil vapor emissions due to engine lubrication systems are possible (Ungeheuer et al., 2022; Bier et al., 2024). This can lead to the nucleation into ultrafine oil droplets, as observed in measurements (Ungeheuer et al., 2021). Experiments by Ponsonby et al. (2024) explored the potential of lubrication oil droplets to act as contrail ice-forming particles, revealing that these droplets are less effective as condensation nuclei than soot particles within the temperature range of 225–245 K. Nevertheless, the study showed that lubrication oil droplets can competitively deplete plume supersaturation under soot-poor conditions, as their critical supersaturation is readily achievable. In H_2 plumes, these ultrafine oil droplets might contribute to ice crystal formation alongside background aerosols. Further research on the properties of oil droplets, such as their size distribution and emission indices, is necessary to fully understand their potential

role in contrail ice crystal formation processes. Yu et al. (2024) highlight that UFPs might significantly contribute to the total number of contrail ice particles if the sizes of the soot particles are reduced. Hence, understanding the role of UFPs in the contrail formation process requires the consideration of both soot emissions and particle sizes. The UFP number could potentially exceed that of emitted soot particles per flight distance, leading to a larger number of nucleated ice crystals in H_2 plumes compared to conventional kerosene plumes (Kärcher et al., 2015; Bier et al., 2024). This justifies our approach of increasing the initial number of ice crystals to capture possible scenarios of additional ice-forming particle sources.

Furthermore, this study addresses a previously unexplored area by analyzing contrail evolution during the vortex phase at temperatures $> 225\,\mathrm{K}$. At higher ambient temperatures, the number of nucleated ice crystals decreases, increasing the number of ice crystals that survive the vortex phase (Bier and Burkhardt, 2022). Since our study design is independent of the specific formation processes, it hypothetically determines the survival fractions for a given fixed N_0.

We revised the original formulation of the vortex loss parametrization by incorporating the conservation of mass mixing ratios, adding a layer of complexity to the equations but ensuring that the physical assumptions are accurately represented. With appropriately chosen parameters, the arc tangent curve fits the data points well, both from the U2016 and present studies. Additionally, the new formulation of the fitting function is designed to account for scenarios where N_0 is significantly upscaled. Although the parametrization is based on the N_0-scaling study spanning four orders of magnitude, it remains applicable even for more extreme values of N_0. The parametrization also yields plausible results in terms of high ambient temperatures. The updated parametrization does not fully capture specific data points, particularly in cases with decreased stratification and downscaled N_0 values. As the length scale z_{desc} is the quantity that accounts for the variation of atmospheric stability, an adjustment to the formulation of z_{desc}, as initially proposed by Unterstrasser (2014), may be necessary to improve accuracy.

Next, we motivate our new choice for the adaptation factor Ψ in the updated ice crystal loss parametrization. The original version in U2016 was based on simulations that all had the same $\mathrm{EI_{H_2O}}$ value, and the emission index $\mathrm{EI_{iceno}}$ was a good estimator of the representative ice crystal size in the contrail. A straightforward generalization would be to replace $\mathrm{EI_{iceno}}$ by the ratio $\mathrm{EI_{H_2O}}/\mathrm{EI_{iceno}}$ in the definition of Ψ. However, this quantity is only a proxy of the ice crystal mean mass $(:= I_0/N_0 = \mathrm{EI_{H_2O}}/\mathrm{EI_{iceno}})$ when all emitted water vapor deposits on the ice crystals, yet it neglects the contribution from the environment. Keeping in mind that the buffering effect of the two water vapor sources (from emission and from environment) is already captured by z_Δ, we now define Ψ as a proxy for the typical ice crystal number concentration in the primary wake. The exact definition can be found in section A1.

One main goal of our study is to understand and systematically analyze the impact of the initial ice crystal number and of an assumed water vapor emission on the early contrail properties. We neglect any possible changes in aircraft geometry, mass, overall propulsion efficiency, etc., between current kerosene-driven aircraft and future H_2 aircraft. Clearly, such adaptations would affect the strength of the wake vortices and the fuel consumption (in addition to the factor 2.79^{-1} mentioned above). Moreover, H_2 fuel cells produce electric power that drives propellers. Design concepts with different numbers and positions of propellers and exhaust outlets exist in the literature (e.g. Marciello et al., 2023; Tiwari et al., 2024). Understanding the formation and the early evolution of contrails behind a propeller-driven aircraft deserves separate modelling studies. For the

time being, we prefer to limit our study to variations of N_0 and I_0 without any other aircraft adaptation in order to avoid complicating and overloading the interpretation of our results.

Once H$_2$ aircraft designs are less hypothetical, one could incorporate such adaptations (like a systematically higher aircraft mass due to larger tank systems or particular aspects of H$_2$ fuel cell aircraft) in subsequent modelling studies.

The updated parametrization is now prepared for integration into large-scale global models, where the U2016 parametrization is already implemented (Bier and Burkhardt, 2022). Bier and Burkhardt (2022) underscore the significance of the initial number of ice crystals, highlighting the critical role of our study, which focuses on the vortex phase and ice crystal loss, in assessing the climate impact of H$_2$ contrails.

5   Conclusions

In this study, we simulated the evolution of contrails up to an age of approximately six minutes using the EULAG-LCM model, a fluid dynamics solver coupled with a particle-based microphysical model. The focus is on contrails produced by hydrogen-powered aircraft, including both hydrogen direct combustion and hydrogen fuel cell systems. The simulations assume that ice crystal formation and vortex roll-up are complete at initialization. We varied the initial number of ice crystals over a wide range spanning four orders of magnitude, from $3.38 \times 10^{10}\,\mathrm{m}^{-1}(0.85 \times 10^{10}\,\mathrm{m}^{-1})$ to $3.38 \times 10^{14}\,\mathrm{m}^{-1}(0.85 \times 10^{14}\,\mathrm{m}^{-1})$ for an A350/B777-like (A320/B737-like) aircraft. Additionally, we scaled the emitted water vapor by a factor of 2.57 compared to the reference kerosene case. A parameter study was conducted, varying meteorological, microphysical, and aircraft parameters, focusing on the survival fraction / final number of ice crystals, a critical factor influencing subsequent contrail evolution.

Our simulations indicate that ice crystals tend to be larger in contrails from hydrogen-powered aircraft, leading to a higher likelihood of surviving the vortex phase. This effect is also observed in contrails initialized with a very small number of ice crystals, where the limited competition for available water vapor during depositional growth promotes the formation of larger ice crystals. As anticipated in previous studies, we find initial differences in ice crystal number getting reduced after the vortex phase. The higher the initial ice crystal number, the stronger this reduction is. This finding is independent of any meteorological condition. Sublimation driven by adiabatic heating in the descending vortex pair becomes more significant in drier atmospheric conditions, a trend consistent across all N_0 variations. Furthermore, a higher ambient temperature enhances ice crystal sublimation, though the surviving crystals tend to be larger. We find that the temperature sensitivity is particularly pronounced in the N_0-upscaling scenarios. A reduced thermal stratification leads to a more significant loss of ice crystals, with this effect being more pronounced at higher initial ice crystal numbers and in drier atmospheric conditions. A shift towards a narrower initial size distribution generally produces larger ice crystal sizes, thereby reducing the extent to which initial differences are balanced, as we have consistently observed in the H$_2$ simulations. The weaker vortex descent associated with smaller aircraft results in a reduced sublimation of ice crystals in the primary wake, leading to higher survival fractions in the case of A320 aircraft. This trend is consistent across all N_0 values and ambient temperature scenarios.

We have refined the existing parametrization of ice crystal loss, presented by Unterstrasser (2016), by incorporating a new set of H$_2$-contrail simulations. Given that the new simulations tend to cluster at the extremes of the parametrization function, we

adjusted the fitting procedure to better capture these behaviors. The updated set of fitting coefficients is provided. A comparison with simulation results from other studies demonstrates a good agreement with our updated parametrization.

It is not yet possible to make a definitive assessment of whether flying with hydrogen is advantageous from a contrail perspective. Further research is needed to assess contrail formation processes for hydrogen propulsion, with measurement results (Airbus, 2023) providing essential insights. As shown in Figs. 10 and 11, the initial number of ice crystals has a significant impact on the subsequent characteristics of the contrail. This study aimed to conduct a broad analysis of N_0 during the first six minutes of contrail evolution. Determining more robustly the number of ice crystals formed in the H_2 case remains an active area of research.

The analysis of the complete set of contrail-cirrus simulations (extending the study that is demonstrated in Sec. 3.4), which are based on the H_2-contrail vortex phase simulations presented here, is in progress.

Appendix A: Details about the ice crystal loss parametrization

A1 Definition of the ice crystal concentration n_0 in the new parametrization

As described in Sec. 3.3, the adaptation factor Ψ accounting for the mean ice crystal size (in the original formulation given by $1/\mathrm{EI}^*_{\mathrm{iceno}}$) is now defined differently. In the new formulation, Ψ is expressed as $\Psi = 1/n_0^*$, where n_0 represents an (intermediate) ice crystal number concentration:

$$n_0 = N_0/A_{\mathrm{p}}, \tag{A1}$$

where N_0 is the initial ice crystal number (per meter of flight path) and A_{p} is the intermediate plume cross-sectional area. Hence, n_0 represents an average concentration in the primary wake. We recall $N_0 = m_{\mathrm{C}} \times \mathrm{EI}_{\mathrm{iceno}}$ (see Eq. (1)) and the empirical relationships (for conventional aircraft designs of different sizes as studied in Unterstrasser and Görsch (2014) and derived in U2016): $m_{\mathrm{C}} \sim b_{\mathrm{span}}{}^2$ (Eq. (A9) in U2016) and $A_{\mathrm{p}} \sim b_{\mathrm{span}}{}^2$ (Eqs. (A6) and (A7) in U2016), where b_{span} is the wing span of the aircraft. Hence, n_0 is roughly independent of aircraft type, but depends linearly on $\mathrm{EI}_{\mathrm{iceno}}$. Note that the empirical relation for A_{p} is derived from the simulation results and is not supposed to be adapted. The actual fuel consumption m_{C} may, however, deviate from the empirical relationship (representing typical kerosene fuels) and should serve as input to the parametrization.

The parametrization was trained such that the kerosene A350 reference simulations serve as reference case for determining $n_{0,\mathrm{ref}}$ and $n_0^* = n_0/n_{0,\mathrm{ref}}$ (with $N_{0,\mathrm{ref}} = 3.38 \times 10^{12}\,\mathrm{m}^{-1}$ and $b_{\mathrm{span,ref}} = 60.3\,\mathrm{m}$). Note that in particular the m_{C} values of our A350 setups deviate from the empirical relationship (see Fig. A1 (c) in U2016), and hence, switching to a smaller A320 aircraft gives a smaller n_0 value ($1.29 \times 10^9\,\mathrm{m}^{-3}$ (A350) vs. $8.93 \times 10^8\,\mathrm{m}^{-3}$ (A320)) leading to $n_0^* = 0.69$.

A2 Differences between the original and new parametrization implementation

This section summarizes the differences between the original parametrization provided in Unterstrasser (2016) and the new one presented in Sec. 3.3. The overall design of the parametrization has not changed, and the cookbook of individual computations, as listed in Sec. A6 of U2016, received only minor changes, which are as follows:

- In step 2, the formula for computing the plume area is now $A_p = 2 \times \pi r_p^2$, which replaces Eq. (A7) of U2016, which was given by $A_p = 4 \times \pi r_p^2$.

- In step 3, z_{atm} and z_{emit} are redefined using now the adiabatic index κ (as given in Eqs. (7) and (8)). Moreover, the bisection method for solving the nonlinear equation can be replaced by analytically defined fit functions provided in the subsequent subsection.

- In steps 3 and 4, new values for the fitting coefficients are used as given in Eqs. (14a)-(14g). Moreover, the adaptation factor Ψ uses a new definition as given in subsection A1.

The supplement contains Fortran and Python implementations of the new and the original parametrization.

A3 Analytical fit functions of z_{atm} and z_{emit}

To compute the length scales z_{atm} and z_{emit} (Eqs. (7) and (8)), we employed so far the numerical bisection method. Here, we present an alternative approach that directly calculates these length scales based on input data for temperature, ambient supersaturation, and water vapor concentration. The corresponding formulae are as follows:

$$\tilde{z}_{atm} = 607.46\,\text{m} \times s_i^{0.897} \times \left(\frac{T_{CA}}{205\,\text{K}} \right)^{2.225} \tag{A2}$$

and

$$\tilde{z}_{emit} = 1106.6\,\text{m} \times \left(\frac{\rho_{emit}}{10\,\text{mg/m}^3} \right)^{0.678 + 0.0116\,T_{205}}$$
$$\times \exp\left((-(0.0807 + 0.000428\,T_{205})\,T_{205}) \right) \tag{A3}$$

with $T_{205} = T_{CA}/\text{K} - 205$.

The resulting length scales show only slight deviations from those derived using the bisection method, with a maximum deviation of 3 m for z_{atm} and 7 m for z_{emit}. Applying the analytical relations to calculate the parametrized survival fraction, we observe no change in 44 % of the data (when rounded to two digits, as done in Tab. A1) and a maximum deviation of 2.0 %. A detailed comparison is provided in Tab. S1. The supplement contains further plots that demonstrate the suitability of the fit functions.

Supplement. The supplement related to this article is available online at:

.

References

Airbus: Towards the world's first hydrogen-powered commercial aircraft, https://www.airbus.com/en/innovation/energy-transition/hydrogen/zeroe#concepts, 2020.

Airbus: Contrail-chasing Blue Condor makes Airbus' first full hydrogen-powered flight, https://www.airbus.com/en/newsroom/stories/2023-11-contrail-chasing-blue-condor-makes-airbus-first-full-hydrogen-powered#, 2023.

Bier, A. and Burkhardt, U.: Impact of Parametrizing Microphysical Processes in the Jet and Vortex Phase on Contrail Cirrus Properties and Radiative Forcing, J. Geophys. Res., 127, e2022JD036 677, https://doi.org/10.1029/2022JD036677, 2022.

Bier, A., Burkhardt, U., and Bock, L.: Synoptic Control of Contrail Cirrus Life Cycles and Their Modification Due to Reduced Soot Number Emissions, J. Geophys. Res., pp. 11 584–11 603, https://doi.org/10.1002/2017JD027011, 2017JD027011, 2017.

Bier, A., Unterstrasser, S., Zink, J., Hillenbrand, D., Jurkat-Witschas, T., and Lottermoser, A.: Contrail formation on ambient aerosol particles for aircraft with hydrogen combustion: a box model trajectory study, Atmos. Chem. Phys., 24, 2319–2344, https://doi.org/10.5194/acp-24-2319-2024, 2024.

Bräuer, T., Voigt, C., Sauer, D., Kaufmann, S., Hahn, V., Scheibe, M., Schlager, H., Huber, F., Le Clerq, P., Moore, R. H., and Anderson, B. E.: Reduced ice number concentrations in contrails from low-aromatic biofuel blends, Atmos. Chem. Phys., 21, 16 817–16 826, https://doi.org/10.5194/acp-21-16817-2021, 2021.

Burkhardt, U. and Kärcher, B.: Global radiative forcing from contrail cirrus, Nature Clim. Ch., 1, 54–58, https://doi.org/10.1038/nclimate1068, 2011.

Burkhardt, U., Bock, L., and Bier, A.: Mitigating the contrail cirrus climate impact by reducing aircraft soot number emissions, npj Climate and Atmospheric Science, 1, 37, https://doi.org/10.1038/s41612-018-0046-4, 2018.

Clark, T. L. and Farley, R. D.: Severe downslope windstorm calculations in two and three spatial dimensions using anelastic interactive grid nesting: a possible mechanism for gustiness., J. Atmos. Sci., 41, 329–350, 1984.

Crow, S.: Stability theory for a pair of trailing vortices, AIAA Journal, 8, 2172–2179, 1970.

Gierens, K.: Theory of Contrail Formation for Fuel Cells, Aerospace, 8, https://doi.org/10.3390/aerospace8060164, 2021.

Gierens, K. and Spichtinger, P.: On the size distribution of ice-supersaturated regions in the upper troposphere and lowermost stratosphere, Ann. Geophys., 18, 499–504, https://doi.org/10.1007/s00585-000-0499-7, 2000.

Gierens, K., Matthes, S., and Rohs, S.: How Well Can Persistent Contrails Be Predicted?, Aerospace, 7, https://doi.org/10.3390/aerospace7120169, 2020.

Gruber, S., Unterstrasser, S., Bechtold, J., Vogel, H., Jung, M., Pak, H., and Vogel, B.: Contrails and their impact on shortwave radiation and photovoltaic power production – a regional model study, Atmos. Chem. Phys., 18, 6393–6411, https://doi.org/10.5194/acp-18-6393-2018, 2018.

Huebsch, W. and Lewellen, D.: Sensitivity Study on Contrail Evolution, 36 th AIAA Fluid Dynamics Conference and Exhibit,, AIAA 2006-3749, 1–14, https://doi.org/10.2514/6.2006-3749, 2006.

Jansen, J. and Heymsfield, A. J.: Microphysics of Aerodynamic Contrail Formation Processes, J. Atmos. Sci., 72, 3293–3308, https://doi.org/10.1175/JAS-D-14-0362.1, 2015.

Kärcher, B.: Formation and radiative forcing of contrail cirrus, Nature Communications, 9, 1824, https://doi.org/10.1038/s41467-018-04068-0, 2018.

Kärcher, B., Burkhardt, U., Bier, A., Bock, L., and Ford, I. J.: The microphysical pathway to contrail formation, J. Geophys. Res., 120, 7893–7927, https://doi.org/10.1002/2015JD023491, 2015.

Kaufmann, S., Dischl, R., and Voigt, C.: Regional and seasonal impact of hydrogen propulsion systems on potential contrail cirrus cover, Atmos. Environ., 24, 100 298, https://doi.org/10.1016/j.aeaoa.2024.100298, 2024.

Kazula, S., de Graaf, S., and Enghardt, L.: Review of fuel cell technologies and evaluation of their potential and challenges for electrified propulsion systems in commercial aviation, Journal of the Global Power and Propulsion Society, 7, 43–57, https://doi.org/10.33737/jgpps/158036, 2023.

Lee, D. S., Fahey, D. W., Skowron, A., Allen, M. R., Burkhardt, U., Chen, Q., Doherty, S. J., Freeman, S., Forster, P. M., Fuglestvedt, J., Gettelman, A., De León, R. R., Lim, L. L., Lund, M. T., Millar, R. J., Owen, B., Penner, J. E., Pitari, G., Prather, M. J., Sausen, R., and Wilcox, L. J.: The contribution of global aviation to anthropogenic climate forcing for 2000 to 2018, Atmos. Environ., 244, 117 834, https://doi.org/10.1016/j.atmosenv.2020.117834, 2021.

Lee, D. S., Allen, M. R., Cumpsty, N., Owen, B., Shine, K. P., and Skowron, A.: Uncertainties in mitigating aviation non-CO2 emissions for climate and air quality using hydrocarbon fuels, Environ. Sci.: Atmos., 3, 1693–1740, https://doi.org/10.1039/D3EA00091E, 2023.

Lewellen, D. and Lewellen, W.: Large-eddy simulations of the vortex-pair breakup in aircraft wakes, AIAA Journal, 34, 2337–2345, 1996.

Lewellen, D. C.: Persistent contrails and contrail cirrus. Part 2: Full Lifetime Behavior, J. Atmos. Sci., pp. 4420–4438, https://doi.org/10.1175/JAS-D-13-0317.1, 2014.

Lewellen, D. C. and Lewellen, W. S.: Effects of aircraft wake dynamics on measured and simulated NOx and HOx wake chemistry, J. Geophys. Res., 106, 27 661–27 672, 2001.

Lewellen, D. C., Meza, O., and Huebsch, W. W.: Persistent contrails and contrail cirrus. Part 1: Large-eddy simulations from inception to demise, J. Atmos. Sci., 71, 4399–4419, https://doi.org/10.1175/JAS-D-13-0316.1, 2014.

Marciello, V., Di Stasio, M., Ruocco, M., Trifari, V., Nicolosi, F., Meindl, M., Lemoine, B., and Caliandro, P.: Design Exploration for Sustainable Regional Hybrid-Electric Aircraft: A Study Based on Technology Forecasts, Aerospace, 10, https://doi.org/10.3390/aerospace10020165, 2023.

Märkl, R. S., Voigt, C., Sauer, D., Dischl, R. K., Kaufmann, S., Harlaß, T., Hahn, V., Roiger, A., Weiß-Rehm, C., Burkhardt, U., Schumann, U., Marsing, A., Scheibe, M., Dörnbrack, A., Renard, C., Gauthier, M., Swann, P., Madden, P., Luff, D., Sallinen, R., Schripp, T., and Le Clercq, P.: Powering aircraft with 100 % sustainable aviation fuel reduces ice crystals in contrails, Atmos. Chem. Phys., 24, 3813–3837, https://doi.org/10.5194/acp-24-3813-2024, 2024.

Marks, T., Dahlmann, K., Grewe, V., Gollnick, V., Linke, F., Matthes, S., Stumpf, E., Swaid, M., Unterstrasser, S., Yamashita, H., and Zumegen, C.: Climate Impact Mitigation Potential of Formation Flight, Aerospace, 8, 14, https://doi.org/10.3390/aerospace8010014, 2021.

Moore, R. H., Thornhill, K. L., Weinzierl, B., Sauer, D., D'Ascoli, E., Kim, J., Lichtenstern, M., Scheibe, M., Beaton, B., Beyersdorf, A. J., Barrick, J., Bulzan, D., Corr, C. A., Crosbie, E., Jurkat, T., Martin, R., Riddick, D., Shook, M., Slover, G., Voigt, C., White, R., Winstead, E., Yasky, R., Ziemba, L. D., Brown, A., Schlager, H., and Anderson, B. E.: Biofuel blending reduces particle emissions from aircraft engines at cruise conditions, Nature, 543, 411–415, https://doi.org/10.1038/nature21420, 2017.

Petzold, A., Kramer, M., Neis, P., Rolf, C., Rohs, S., Berkes, F., Smit, H. G. J., Gallagher, M., Beswick, K., Lloyd, G., Baumgardner, D., Spichtinger, P., Nedelec, P., Ebert, V., Buchholz, B., Riese, M., and Wahner, A.: Upper tropospheric water vapour and its interaction with cirrus clouds as seen from IAGOS long-term routine in situ observations, Faraday Discuss., 200, 229–249, https://doi.org/10.1039/C7FD00006E, 2017.

Picot, J., Paoli, R., Thouron, O., and Cariolle, D.: Large-eddy simulation of contrail evolution in the vortex phase and its interaction with atmospheric turbulence, Atmos. Chem. Phys., 15, 7369–7389, https://doi.org/10.5194/acp-15-7369-2015, 2015.

730 Ponsonby, J., King, L., Murray, B. J., and Stettler, M. E. J.: Jet aircraft lubrication oil droplets as contrail ice-forming particles, Atmos. Chem. Phys., 24, 2045–2058, https://doi.org/10.5194/acp-24-2045-2024, 2024.

Prusa, J., Smolarkiewicz, P., and Wyszogrodzki, A.: EULAG, a computational model for multiscale flows, Comput. Fluids, 37, 1193–1207, https://doi.org/10.1016/j.compfluid.2007.12.001, 2008.

Schumann, U.: On conditions for contrail formation from aircraft exhausts, Meteorol. Z., 5, 4–23, https://doi.org/10.1127/metz/5/1996/4, 735 1996.

Schumann, U., Mayer, B., Gierens, K., Unterstrasser, S., Jessberger, P., Petzold, A., Voigt, C., and Gayet, J.-F.: Effective Radius of Ice Particles in Cirrus and Contrails, J. Atmos. Sci., 68, 300–321, https://doi.org/10.1175/2010JAS3562.1, 2011.

Smolarkiewicz, P. and Margolin, L.: On forward-in-time differencing for fluids: an Eulerian/semi-Lagrangian non-hydrostatic model for stratified flows, Atmosphere-Ocean Special, 35, 127–152, 1997.

740 Sölch, I. and Kärcher, B.: A large-eddy model for cirrus clouds with explicit aerosol and ice microphysics and Lagrangian ice particle tracking, Q. J. R. Meteorol. Soc., 136, 2074–2093, https://doi.org/10.1002/qj.689, 2010.

Sussmann, R. and Gierens, K.: Lidar and numerical studies on the different evolution of vortex pair and secondary wake in young contrails, J. Geophys. Res., 104, 2131–2142, 1999.

Tiwari, S., Pekris, M. J., and Doherty, J. J.: A review of liquid hydrogen aircraft and propulsion technologies, International Journal of 745 Hydrogen Energy, 57, 1174–1196, https://doi.org/10.1016/j.ijhydene.2023.12.263, 2024.

Ungeheuer, F., van Pinxteren, D., and Vogel, A. L.: Identification and source attribution of organic compounds in ultrafine particles near Frankfurt International Airport, Atmos. Chem. Phys., 21, 3763–3775, https://doi.org/10.5194/acp-21-3763-2021, 2021.

Ungeheuer, F., Caudillo, L., Ditas, F., Simon, M., van Pinxteren, D., Kilic, D., Rose, D., Jacobi, S., Kürten, A., Curtius, J., and Vogel, A. L.: Nucleation of jet engine oil vapours is a large source of aviation-related ultrafine particles, Commun. Earth Environ., 3, 1–8, 750 https://doi.org/10.1038/s43247-022-006, 2022.

Unterstrasser, S.: Large eddy simulation study of contrail microphysics and geometry during the vortex phase and consequences on contrail-to-cirrus transition, J. Geophys. Res., 119, 7537–7555, https://doi.org/10.1002/2013JD021418, 2014.

Unterstrasser, S.: Properties of young contrails - a parametrisation based on large-eddy simulations, Atmos. Chem. Phys., 16, 2059–2082, https://doi.org/10.5194/acp-16-2059-2016, 2016.

755 Unterstrasser, S.: The Contrail Mitigation Potential of Aircraft Formation Flight Derived from High-Resolution Simulations, Aerospace, 7, 170, https://doi.org/10.3390/aerospace7120170, 2020.

Unterstrasser, S. and Gierens, K.: Numerical simulations of contrail-to-cirrus transition - Part 2: Impact of initial ice crystal number, radiation, stratification, secondary nucleation and layer depth, Atmos. Chem. Phys., 10, 2037–2051, https://doi.org/10.5194/acp-10-2037-2010, 2010.

760 Unterstrasser, S. and Görsch, N.: Aircraft-type dependency of contrail evolution, J. Geophys. Res., 119, 14,015–14,027, https://doi.org/10.1002/2014JD022642, 2014.

Unterstrasser, S. and Sölch, I.: Study of contrail microphysics in the vortex phase with a Lagrangian particle tracking model, Atmos. Chem. Phys., 10, 10 003–10 015, https://doi.org/10.5194/acp-10-10003-2010, 2010.

Unterstrasser, S. and Stephan, A.: Far field wake vortex evolution of two aircraft formation flight and implications on young contrails, 765 Aeronaut. J., 124, 667–702, https://doi.org/10.1017/aer.2020.3, 2020.

31

Unterstrasser, S., Paoli, R., Sölch, I., Kühnlein, C., and Gerz, T.: Dimension of aircraft exhaust plumes at cruise conditions: effect of wake vortices, Atmos. Chem. Phys., 14, 2713–2733, https://doi.org/10.5194/acp-14-2713-2014, 2014.

Unterstrasser, S., Gierens, K., Sölch, I., and Lainer, M.: Numerical simulations of homogeneously nucleated natural cirrus and contrail-cirrus. Part 1: How different are they?, Meteorol. Z., 26, 621–642, https://doi.org/10.1127/metz/2016/0777, 2017a.

770   Unterstrasser, S., Gierens, K., Sölch, I., and Wirth, M.: Numerical simulations of homogeneously nucleated natural cirrus and contrail-cirrus. Part 2: Interaction on local scale, Meteorol. Z., 26, 643–661, https://doi.org/10.1127/metz/2016/0780, 2017b.

Voigt, C., Kleine, J., Sauer, D., Moore, R. H., Bräuer, T., Le Clercq, P., Kaufmann, S., Scheibe, M., Jurkat-Witschas, T., Aigner, M., Bauder, U., Boose, Y., Borrmann, S., Crosbie, E., Diskin, G. S., DiGangi, J., Hahn, V., Heckl, C., Huber, F., Nowak, J. B., Rapp, M., Rauch, B., Robinson, C., Schripp, T., Shook, M., Winstead, E., Ziemba, L., Schlager, H., and Anderson, B. E.: Cleaner burning aviation fuels can

775   reduce contrail cloudiness, Commun. Earth Environ., 2, 114, https://doi.org/10.1038/s43247-021-00174-y, 2021.

Wölk, J. and Strey, R.: Homogeneous Nucleation of H2O and D2O in Comparison: The Isotope Effect, The Journal of Physical Chemistry B, 105, 11 683–11 701, https://doi.org/10.1021/jp0115805, 2001.

Yu, F., Kärcher, B., and Anderson, B. E.: Revisiting Contrail Ice Formation: Impact of Primary Soot Particle Sizes and Contribution of Volatile Particles, Environ. Sci. Technol., 58, 17 650–17 660, https://doi.org/10.1021/acs.est.4c04340, 2024.

Nr	AC	T_{CA} (K)	$RH_{i,amb}$ (%)	N_{BV} ($10^{-2}\,s^{-1}$)	N_0 #sim	I_0 (g m^{-1})	r_{SD}	$f_{N,s}$	$\bar{f}_{N,s}$	z_{atm} (m)	z_{emit} (m)	$\hat{z}_{desc}$ (m)
1,2,3,4,5	A350	217	120	1.15	5	15.0	3.0	0.05, 0.23, 0.65, 0.89, 0.98	0.06, 0.23, 0.6, 0.87, 0.97	164	249	339
6,7,8,9,10	A350	217	110	1.15	5	15.0	3.0	0.02, 0.1, 0.28, 0.46, 0.71	0.0, 0.06, 0.22, 0.58, 0.86	85	249	339
11,12,13,14,15,16	A350	217	120	1.15	6	38.55	3.0	0.02, 0.09, 0.39, 0.85, 0.98, 1.0	0.05, 0.2, 0.57, 0.85, 0.96, 1.0	164	546	339
17,18,19,20,21	A350	217	110	1.15	5	38.55	3.0	0.07, 0.27, 0.63, 0.81, 0.92	0.08, 0.29, 0.68, 0.9, 0.98	85	546	339
22,23,24	A350	217	120	1.15	3	15.0	1.0	0.07, 0.88, 1.0	0.06, 0.6, 0.97	164	249	339
25,26,27	A350	217	120	1.15	3	15.0	4.0	0.05, 0.61, 0.98	0.06, 0.6, 0.97	164	249	339
28,29,30	A350	217	110	1.15	3	15.0	1.0	0.05, 0.49, 0.93	0.0, 0.21, 0.86	85	249	339
31,32,33	A350	217	110	1.15	3	15.0	4.0	0.02, 0.26, 0.67	0.0, 0.22, 0.86	85	249	339
34,35,36	A350	217	120	1.15	3	38.55	4.0	0.18, 1.0, 1.0	0.2, 0.85, 1.0	164	546	339
37,38,39	A350	217	110	1.15	3	38.55	4.0	0.09, 0.81, 0.99	0.2, 0.85, 1.0	85	546	339
40,41,42	A350	217	110	1.15	3	38.55	1.0	0.18, 0.92, 1.0	0.08, 0.68, 0.98	85	546	339
43,44,45	A350	217	110	1.15	3	38.55	4.0	0.06, 0.58, 0.89	0.08, 0.68, 0.98	85	546	339
46,47,48	A350	217	120	0.5	3	15.0	3.0	0.02, 0.28, 0.66	0.0, 0.26, 0.94	164	249	515
49,50,51	A350	217	110	0.5	3	15.0	3.0	0.01, 0.1, 0.31	0.0, 0.02, 0.73	85	249	515
52,53,54	A350	217	120	0.5	3	38.55	3.0	0.04, 0.46, 0.84	0.02, 0.71, 1.0	164	546	515
55,56,57	A350	217	110	0.5	3	38.55	3.0	0.02, 0.26, 0.53	0.0, 0.36, 0.96	85	546	515
Simulations at higher ambient temperatures												
58,59,60,61,62	A350	225	120	1.15	5	15.0	3.0	0.02, 0.12, 0.45, 0.76, 0.95	0.03, 0.14, 0.44, 0.79, 0.94	177	110	339
63,64,65,66,67	A350	225	110	1.15	5	15.0	3.0	0.01, 0.04, 0.13, 0.25, 0.45	0.0, 0.01, 0.09, 0.3, 0.69	92	110	339
68,69,70,71,72	A350	225	120	1.15	5	38.55	3.0	0.04, 0.21, 0.63, 0.9, 0.99	0.08, 0.28, 0.67, 0.9, 0.98	177	262	339
73,74,75,76,77	A350	225	110	1.15	5	38.55	3.0	0.02, 0.1, 0.29, 0.46, 0.68	0.0, 0.07, 0.27, 0.65, 0.89	92	262	339
78,79,80,81,82	A350	230	120	1.15	5	38.55	3.0	0.03, 0.15, 0.51, 0.83, 0.97	0.05, 0.21, 0.57, 0.86, 0.97	186	163	339
83,84,85,86,87	A350	230	110	1.15	5	38.55	3.0	0.01, 0.05, 0.17, 0.31, 0.52	0.0, 0.03, 0.15, 0.46, 0.81	97	163	339
88,89,90,91,92	A350	233	120	1.15	5	38.55	3.0	0.02, 0.12, 0.45, 0.78, 0.97	0.05, 0.19, 0.53, 0.84, 0.96	191	123	339
93,94,95,96,97	A350	233	110	1.15	5	38.55	3.0	0.01, 0.04, 0.14, 0.26, 0.45	0.0, 0.02, 0.12, 0.38, 0.76	99	123	339
98,99,100	A350	233	120	1.15	3	38.55	1.0	0.03, 0.63, 1.0	0.04, 0.53, 0.96	191	123	339
101,102,103	A350	233	120	1.15	3	38.55	4.0	0.02, 0.43, 0.96	0.05, 0.53, 0.96	191	123	339
104,105,106	A350	233	110	1.15	3	38.55	1.0	0.01, 0.25, 0.59	0.0, 0.12, 0.76	99	123	339
107,108,109	A350	233	110	1.15	3	38.55	4.0	0.01, 0.12, 0.43	0.0, 0.12, 0.76	99	123	339
110,111,112,113,114	A350	235	120	1.15	5	38.55	3.0	0.02, 0.11, 0.43, 0.75, 0.95	0.04, 0.18, 0.52, 0.83, 0.96	195	102	339
115,116,117,118,119	A350	235	110	1.15	5	38.55	3.0	0.01, 0.03, 0.12, 0.23, 0.42	0.0, 0.01, 0.1, 0.34, 0.73	101	102	339
Simulations with A320/B737-like aircraft												
120	A320	217	120	1.15	1	3.7	3.0	0.89	0.72	164	176	231
121,122,123	A320	225	120	1.15	3	3.7	3.0	0.05, 0.78, 1.0	0.13, 0.64, 0.96	177	76	231
124,125,126	A320	225	110	1.15	3	3.7	3.0	0.01, 0.29, 0.86	0.03, 0.21, 0.78	92	76	231
127,128,129	A320	225	120	1.15	3	9.51	3.0	0.07, 0.85, 1.0	0.2, 0.76, 0.99	177	185	231
130,131,132	A320	225	110	1.15	3	9.51	3.0	0.03, 0.52, 0.96	0.07, 0.39, 0.9	92	185	231
133,134,135	A320	230	120	1.15	3	9.51	3.0	0.05, 0.8, 1.0	0.17, 0.72, 0.98	186	114	231
136,137,138	A320	230	120	1.15	3	9.51	3.0	0.02, 0.35, 0.88	0.04, 0.29, 0.85	186	114	231
139,140,141	A320	233	120	1.15	3	9.51	3.0	0.04, 0.78, 1.0	0.16, 0.71, 0.97	191	85	231
142,143,144	A320	233	110	1.15	3	9.51	3.0	0.01, 0.3, 0.86	0.04, 0.26, 0.82	99	85	231
145,146,147	A320	235	120	1.15	3	9.51	3.0	0.04, 0.76, 1.0	0.16, 0.7, 0.97	195	70	231
148,149,150	A320	235	110	1.15	3	9.51	3.0	0.01, 0.27, 0.84	0.03, 0.24, 0.81	101	70	231

Table A1. Summary of the simulations performed. Columns 3–5 list the meteorological parameters, while columns 6–8 present the microphysical initialization settings. Columns 9 and 10 display both the simulated and parametrized survival fractions. Lastly, columns 11–13 specify the length scales employed in the parametrization. Rows showing five simulations correspond to sets with N_0-scaling factors of 100, 10, 1, 0.1, and 0.01. Rows showing three simulations represent sets with scaling factors of 100, 1, and 0.01. In the third row, a total of six simulations are included, with simulation 11 performed using a scaling factor of 1000.